iScience

CellPress

Article

Photo-Enhanced Singlet Oxygen Generation of Prussian Blue-Based Nanocatalyst for Augmented Photodynamic Therapy

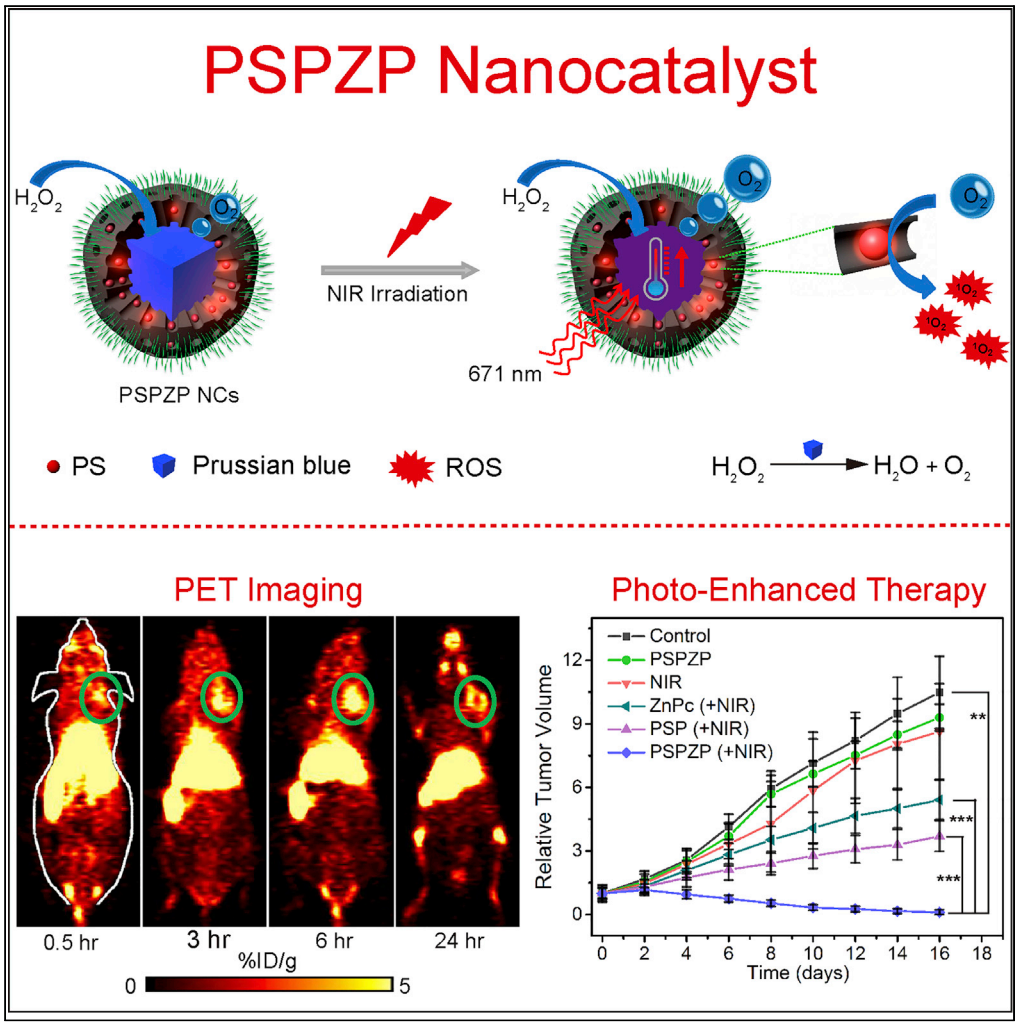

Dongdong Wang, Ruohong Shi, Jiajia Zhou, ..., Weibo Cai, Zhen Guo, Qianwang Chen

hw39@hmfl.ac.cn (H.W.)
wcai@uwhealth.org (W.C.)
zhenguo@ustc.edu.cn (Z.G.)
cqw@ustc.edu.cn (Q.C.)

HIGHLIGHTS

All compositions have been approved by the US Food and Drug Administration

PSP-^{89}Zr serves as a dual-modal PET and PAI imaging agent

PSP shows catalase-like activity toward H_2O_2 decomposition under tumor-microenvironment

Photo-enhanced endogenous O_2 generation of PSPZP for augmented photodynamic therapy

Wang et al., iScience 9, 14–26 November 30, 2018
https://doi.org/10.1016/j.isci.2018.10.005

iScience

CellPress

Article

Photo-Enhanced Singlet Oxygen Generation of Prussian Blue-Based Nanocatalyst for Augmented Photodynamic Therapy

Dongdong Wang,[1] Ruohong Shi,[1] Jiajia Zhou,[2] Sixiang Shi,[3] Huihui Wu,[2] Pengping Xu,[1] Hui Wang,[4,*] Guoliang Xia,[1] Todd E. Barnhart,[3] Weibo Cai,[3,*] Zhen Guo,[2,*] and Qianwang Chen[1,4,5,*]

SUMMARY

Therapeutic effects of photodynamic therapy (PDT) remain largely limited because of tumor hypoxia. Herein, we report safe and versatile nanocatalysts (NCs) for endogenous oxygen generation and imaging-guided enhanced PDT. The NCs (named as PSP) are prepared by coating Prussian blue (PB) with mesoporous silica to load photosensitizer (zinc phthalocyanine, ZnPc), followed by the modification of polyethylene glycol chains. The inner PB not only acts like a catalase for hydrogen peroxide decomposition but also serves as a photothermal agent to increase the local temperature and then speed up the oxygen supply under near-infrared irradiation. The loaded ZnPc can immediately transform the formed oxygen to generate cytotoxic singlet oxygen upon the same laser irradiation due to the overlapped absorption between PB and ZnPc. Results indicate that the PSP-ZnPc (PSPZP) NCs could realize the photothermally controlled improvement of hypoxic condition in cancer cells and tumor tissues, therefore demonstrating enhanced cancer therapy by the incorporation of PDT and photothermal therapy.

INTRODUCTION

As a minimally invasive and toxic strategy, photodynamic therapy (PDT) has been popularly studied in clinical fields for localized and superficial cancer treatment (Hopper, 2000; Lucky et al., 2015; Straten et al., 2017). PDT is easily performed; it utilizes a light source to activate the administered photosensitizing molecules conjugated with molecular oxygen (O_2) to generate cytotoxic singlet oxygen ($^1O_2$) or other kinds of reactive oxygen species (ROS) to induce cell death (Brown et al., 2004; Dolmans et al., 2003; Huang et al., 2012; Zhang et al., 2008). In addition to directly killing cancer cells, PDT appears to shrink or destroy tumors by damaging blood vessels in the tumor or by activating the immune system to attack cancer cells (Dougherty et al., 1998; Juarranz et al., 2008). The O_2-involved therapeutic effect of PDT has remarkably improved the selectivity and side effects of traditional therapeutic agents for cancer therapy (Abbas et al., 2017; Noh et al., 2018; Tian et al., 2011). However, the efficiency of PDT is always limited by the rapid O_2 consumption because of the O_2-dependent treatment process (Jin et al., 2013; Mitchell et al., 1985; See et al., 1984). More importantly, the rapid proliferation of cancer cells as well as the distorted tumor blood vessels would further lower the O_2 supply, leading to hypoxia in the tumor site and hindering the O_2-involved cancer therapy (Bristow and Hill, 2008; Vander Heiden et al., 2009; Xu et al., 2016; Yang et al., 2017; Zhang et al., 2015).

Over the past decade, two strategies have been mainly explored for enhancing O_2 supply against pre-existing hypoxia in the tumor site. One is to increase the O_2 concentration in the tumor site by applying intelligent nanoparticles (NPs) to deliver O_2 during blood circulation (Chen et al., 2017; Cheng et al., 2015). The other one is to directly produce O_2 in the tumor site by using NPs to catalyze abundant hydrogen peroxide (H_2O_2, usually ranging from 100 μM to 1 mM) in cancer cells resulting from the excess ROS due to tumor hypoxia (Kuang et al., 2011; Szatrowski and Nathan, 1991). Up to now, all kinds of NP-based nanocatalysts (NCs) have been used for H_2O_2 decomposition and O_2 generation to relieve the tumor hypoxia, such as MnO_2, CaO_2, carbon nitride (C_3N_4), carbon dot, and biological catalase (Chen et al., 2015a; Cheng et al., 2016; Fan et al., 2015; Huang et al., 2016; Jia et al., 2018; Zheng et al., 2016). The NCs demonstrate an excellent activity for increasing endogenous O_2 supply, and therefore could generate more cytotoxic $^1O_2$ for increase in cancer cell death under near-infrared (NIR) irradiation (Ge et al., 2014). Although NC-based PDT has shown great potential for cancer treatment, the excess use of photosensitizers to ensure decent therapeutic efficacy still causes severe side effects, including strong light sensitivity and

[1]Hefei National Laboratory for Physical Science at Microscale and Department of Materials Science & Engineering, University of Science & Technology of China, Hefei, Anhui 230026, PR China

[2]Anhui Key Laboratory for Cellular Dynamics and Chemical Biology, School of Life Sciences, University of Science & Technology of China, Hefei, Anhui 230026, PR China

[3]Departments of Radiology and Medical Physics, University of Wisconsin-Madison, Madison, WI 53705, USA

[4]The Anhui Key Laboratory of Condensed Matter Physics at Extreme Conditions, High Magnetic Field Laboratory, Hefei Institutes of Physical Science, Chinese Academy of Sciences, Hefei 230031, PR China

[5]Lead Contact

*Correspondence: hw39@hmfl.ac.cn (H.W.), wcai@uwhealth.org (W.C.), zhenguo@ustc.edu.cn (Z.G.), cqw@ustc.edu.cn (Q.C.)

https://doi.org/10.1016/j.isci.2018.10.005

multiple pain in patients (Calixto et al., 2016; Triesscheijn et al., 2006). Meanwhile, the unpredictable toxicities and uncontrollable catalytic processes of the reported NCs obviously limits their clinical application (Brohi et al., 2017; Romero-Castillo et al., 2017; Srivastava et al., 2015). Thus there is an urgent demand for the development of biocompatible NCs that exhibit stimuli-responsive O_2 supply and simultaneously transform O_2 to cytotoxic $^1O_2$ for enhanced PDT efficiency in a synergistic manner.

Here, we report a safe multifunctional platform as NC for photo-controlled O_2 generation from endogenous H_2O_2 decomposition and imaging-guided photo-enhanced cancer therapy. All compositions in the NCs have been approved by the US Food and Drug Administration (FDA). Prussian blue (PB) is selected as the building block due to its imaging function and catalase-like activity for H_2O_2 decomposition (Cheng et al., 2014; Yang et al., 2012, 2018). It is also expected to control the H_2O_2 decomposition by local temperature variation of PB irradiated with NIR laser because of the photothermal conversion ability of PB NPs. Mesoporous silica is used to coat PB NPs and provide a space for the loading of targeted molecules. After being modified with polyethylene glycol (PEG) molecules, the resultant PB@SiO_2-PEG (named as PSP) NCs will possess good aqueous stability, excellent biocompatibility, and long blood circulation time. Zinc phthalocyanine (ZnPc) is chosen as a photosensitizer model because of its overlapping maximum NIR absorption with PB NPs, which can avoid the time interval between photothermal conversion and PDT of NCs (Lin et al., 2013; Mou et al., 2016). Both *in vitro* and *in vivo* results show that the PSP-ZnPc (PSPZP) NCs can enhance photodynamic efficacy for cancer therapy under NIR irradiation since the increase in local temperature of photo-enhanced NCs could improve *in situ* O_2 generation at the tumor site.

RESULTS

Preparation and Characterization of the PSPZP NCs

Figure 1A demonstrates the synthetic process of multifunctional PSP NCs with enhanced photo-induced O_2 and $^1O_2$ generation. The PB template NPs (see Transparent Methods) possess a uniform size distribution (~80 nm) and cube-like shape (Figures 1B and S1). After being coated with mesoporous silica through the Stöber method, the as-obtained PB@SiO_2 NPs demonstrate a core-shell structure with an average size of 100 nm (Figure 1C). Powder X-ray diffraction pattern and Fourier transform infrared spectroscopy (Figures S2 and S3) confirmed the successful coating of silica on the surface of PB template as evidenced by the existence of asymmetric stretching (1,082 cm^{-1}) and symmetric vibration (797 cm^{-1}) of Si-O-Si and Si-OH (950 cm^{-1}) (Wang et al., 2015). The PB@SiO_2 NPs were further functionalized with amino groups (-NH_2) with (3-aminopropyl)triethoxysilane, followed by PEGylation with Mal-PEG-SCM (SCM: succinimide; and Mal: maleimide) via amino-SCM click reaction, leading to the formation of biocompatible PSP NCs.

Transmission electron microscopy (TEM) (Figure 1D) shows that PSP NCs have a good monodispersity with an average size of 120 nm. The elemental mapping data (Figure 1E) of single PSP NCs show that the elements of Fe and N are mainly distributed in the core, whereas Si and O are homogenously distributed in the shell, indicating its core-shell shape with a PB core and SiO_2 shell. The hydrodynamic diameter distribution (~140 nm) of PSP NCs measured by dynamic light scattering is slightly larger than that measured by TEM because of the presence of PEG chains on the surface of NCs (Figure S4). The variation of zeta potential of PB@SiO_2 (-32.5 ± 4.3 mV) and PSP NCs (3.2 ± 2.2 mV) reveals that the PEG chains had been successfully immobilized onto the surface of silica (Figure S5). The PEG modification endows excellent stability to the NCs in PBS and saline solutions even after being stored for 20 months (Figure S6).

Figure 2A manifests the UV/visible (Vis) absorption spectra of the PB, PSP, ZnPc, and PSPZP NCs. The great overlap between PSP NCs and ZnPc enables PSPZP to function as a combined photothermal/photodynamic agent under the same excitation wavelength using a single NIR laser. Figure 2B shows the photo-induced temperature increase of PSP NCs at different concentrations. Upon 10-min NIR irradiation (671 nm, 0.4 W cm^{-2}), the temperature of the PSP solution (200 ppm) is raised by 25°C, which confirmed the photothermal conversion of PSP NCs (Su et al., 2016; Tian et al., 2017). The UV/Vis absorption spectra of PSP NCs after six heating-cooling cycles have similar intensity, indicating the remarkable stability of NCs under NIR irradiation (Figures S7 and S8). To investigate the ability of PSP NCs for photo-enhanced H_2O_2 decomposition due to the photothermal conversion of NCs, we carried out time-dependent H_2O_2 assay under different temperatures. As shown in Figure 2C, more than 50% of H_2O_2 can be decomposed within 1 hr at room temperature (25°C). The immediate formation of abundant O_2 bubbles also reveals the strong catalytic capability of PSP NCs once the NCs were added into H_2O_2 solution (Figure 2C, inset). With the increase in aqueous temperature (from 25°C to 43°C), the decomposition rate of H_2O_2 showed an obvious

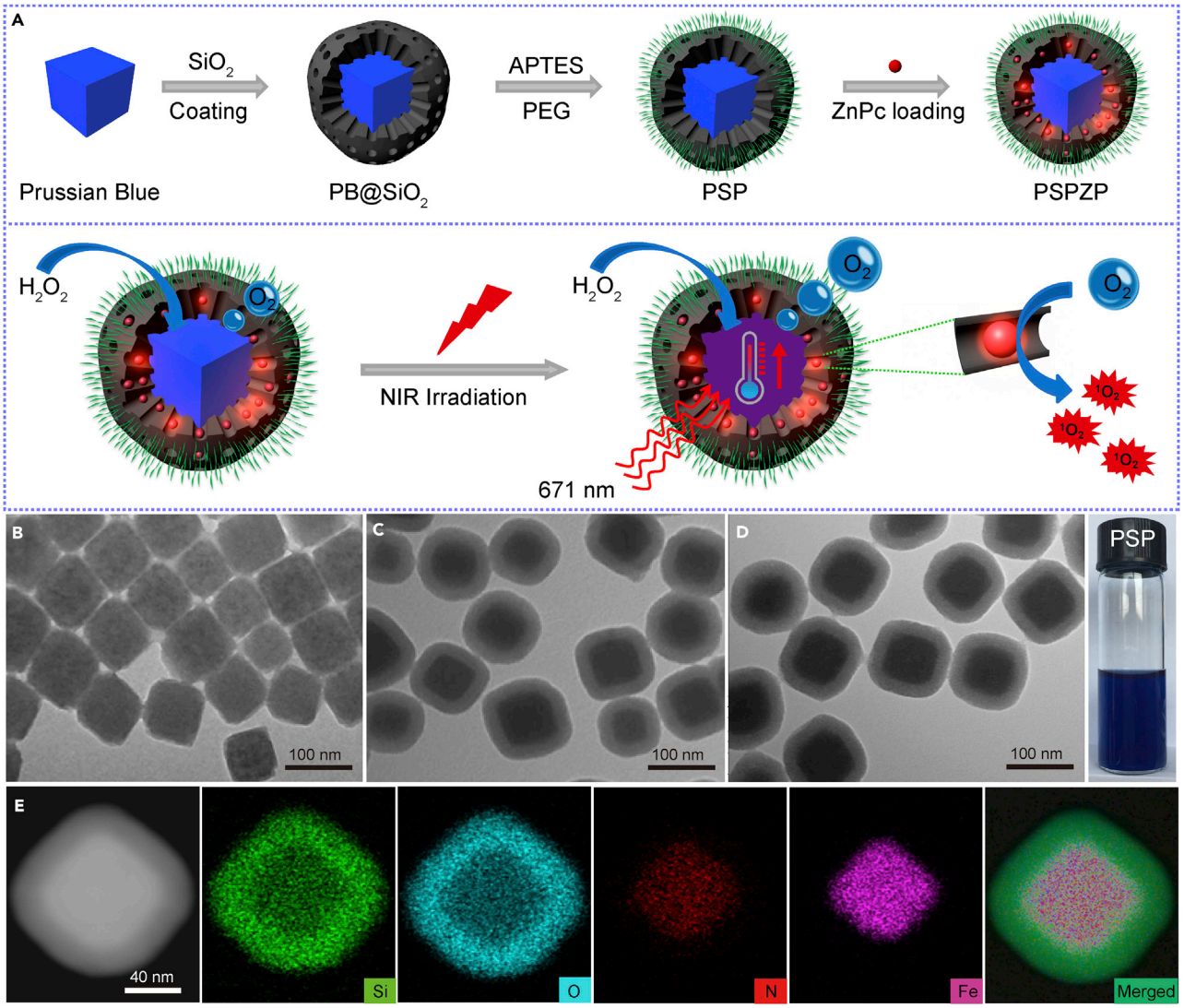

Figure 1. Synthesis and Characterization of the PSP NCs

(A) Schematic of the synthetic procedure and photo-enhanced therapy of the PSPZP NCs.

(B–D) Transmission electron micrographs of (B) PB NPs, (C) PB@SiO_2 NPs, and (D) PSP NCs. The photograph at the right side in (D) shows aqueous PSP dispersion in a vial.

(E) The elemental (Si, O, N, Fe) mappings of PSP NCs.

trend of growth. As we know the decomposition reaction of H_2O_2 is a first-order reaction. The calculated catalytic reaction rate constant under 43°C is 0.0335 min^{-1}, which is 1.93 times than that under 25°C (0.0174 min^{-1}). The generated O_2 was measured by an oxygen probe (JPBJ-608 portable Dissolved Oxygen Meters, Shanghai REX Instrument Factory) (Figure 2D). The result showed that the concentration of dissolved O_2 at 43°C is 1.95 times that at 25°C. Such improved H_2O_2 decomposition at higher temperature would make for the increase in PDT efficiency of PSP NCs due to the accelerated O_2 supply. Furthermore, the catalytic activity of the PSP NCs has no obvious change after repetitive H_2O_2 decomposition (Figure 2E), indicating their excellent catalytic stability.

Characterization of Photothermal and Photodynamic Efficacy

Full nitrogen sorption isotherms were obtained to measure the porous properties of PSP NCs. As shown in Figure S9, the Brunauer-Emmett-Teller surface area, pore volume, and pore size of PSP NCs are 427.6 $m^2 g^{-1}$, 0.375 $cm^3 g^{-1}$, and 2.82 nm, respectively. The mesoporous shell and large surface area of

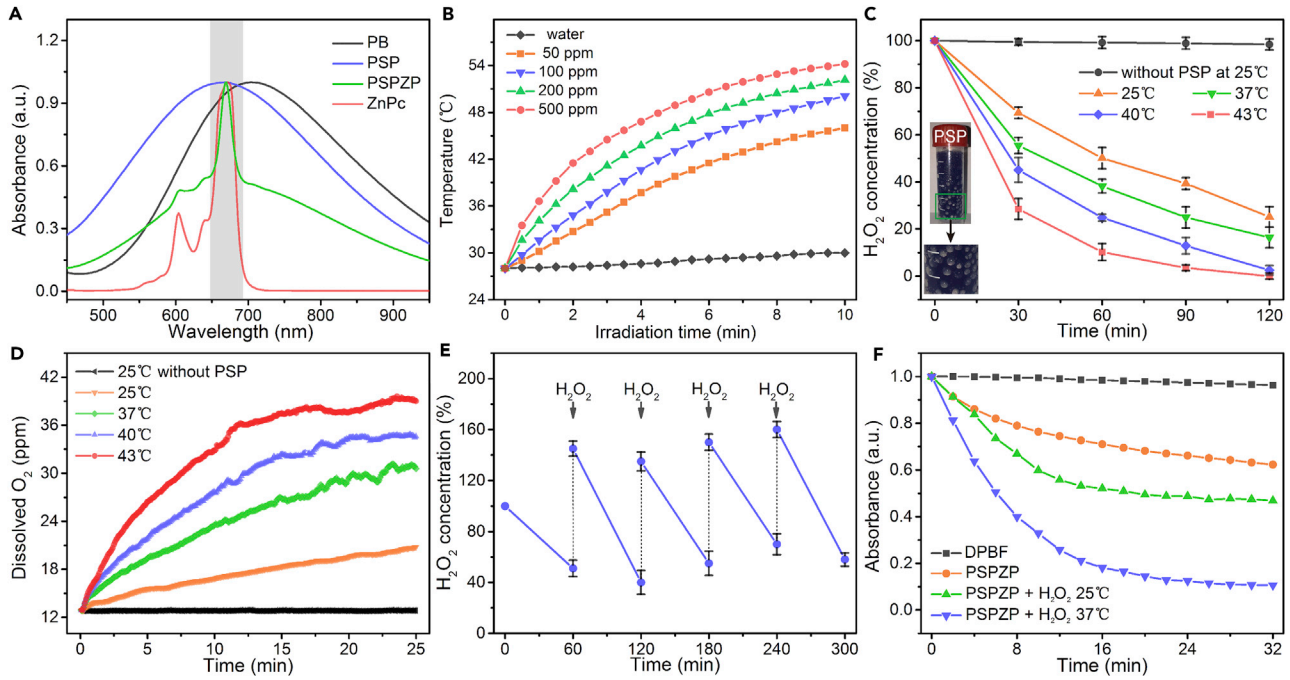

Figure 2. Characterization of Photothermal and Photodynamic Efficacies

(A) UV/Vis absorption spectra of PB, PSP, ZnPc, and PSPZP (dispersed in DMSO).

(B) Temporal temperature evolutions of PSP solutions at various concentrations under NIR irradiation (671 nm, 0.4 W cm^{-2}).

(C and D) Decomposition (C) and O_2 generation (D) of H_2O_2 treated with PSP NCs or not treated under various temperatures (25°C, 37°C, 40°C, and 43°C).

(E) The catalytic ability of PSP NCs with repetitive addition of H_2O_2 at room temperature.

(F) Singlet oxygen generation efficiency determined by 1,3-diphenylisobenzonfuran (DPBF) under various conditions.

Error bars were based on the standard error (mean ± SEM, n = 3).

PSP NCs make them suitable as carriers for photosensitizer loading. The loading capacity was determined by calculating the absorbance change of the characteristic absorption peak of ZnPc (Figure S10). Results showed that each PSP particle could load about 18,800 ZnPc molecules. Given the effective catalytic ability of PSP for O_2 generation, PSPZP NCs have great potential as $^1O_2$ supplier for PDT. The produced $^1O_2$ was determined by measuring the bleaching of 1,3-diphenylisobenzonfuran at 421 nm under Ar atmosphere. Notably, in comparison with the absence of H_2O_2, a significant increase in $^1O_2$ generation by PSPZP was observed in the presence of H_2O_2 (Figure 2F) at room temperature. Since the inert atmosphere has completely maintained the hypoxic condition in catalytic system, the increased $^1O_2$ generation should come from PSPZP-induced H_2O_2 decomposition and O_2 generation. Importantly, the $^1O_2$ generation can be controlled through the variation of local temperature (from 25°C to 37°C), indicating that the PDT efficiency of PSPZP NCs should be improved by the photo-induced temperature change resulting from the photothermal conversion effect of NCs under NIR irradiation.

Before conducting the PDT of PSPZP *in vitro*, the endogenous H_2O_2 decomposition and O_2 generation of PSP NCs was assessed. As shown in Figure 3A, strong green fluorescence shows the high H_2O_2 level in 4T1 cells in hypoxic condition when treated with 100 μM H_2O_2. The decrease in fluorescence intensity of the cells treated with PSP NCs indicated that the PSP could efficiently perform endogenous H_2O_2 decomposition. The disappearance of fluorescence intensity of the cells treated with PSP NCs under NIR irradiation further showed that the external laser could speed up the H_2O_2 decomposition. In addition, to further evaluate the O_2 generation *in vitro*, an O_2 indicator $[Ru(dpp)_3]Cl_2$ was applied to monitor the endogenous O_2 level (Figure 3B). 4T1 cells incubated under hypoxia condition exhibited the strongest red fluorescence intensity due to the insufficient O_2 supply. After being treated with PSP NCs, the reduction in the fluorescence intensity indicates O_2 generation due to endogenous H_2O_2 decomposition, especially with the addition of NIR irradiation. The aforementioned results reveal that PSP NCs can significantly alleviate endogenous hypoxia *in vitro* via *in situ* H_2O_2 decomposition and O_2 generation under NIR irradiation. The cytotoxicities of PSP and PSPZP NCs with/without NIR irradiation under hypoxic and normoxic

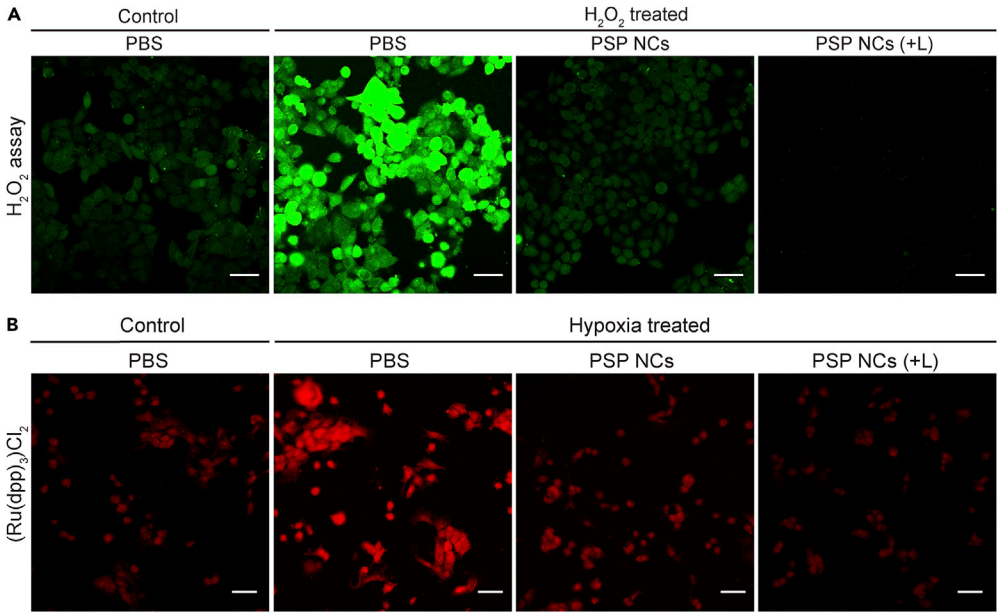

Figure 3. Enhanced H_2O_2 Decomposition and O_2 Generation of PSP NCs in Cells

(A) Confocal laser scanning microscopy (CLSM) images of green fluorescent intracellular H_2O_2 in 4T1 cells incubated with PBS or PSP NCs treated or not treated by NIR irradiation. Scale bar, 50 μm.

(B) CLSM images of 4T1 cells stained with O_2 indicator ($(Ru(dpp)_3)Cl_2$) after different treatments (normoxia with PBS as control, hypoxia with PBS, hypoxia with PSP NCs, and hypoxia with PSP NCs plus NIR irradiation). Scale bar, 50 μm.

conditions were evaluated. As shown in Figure S11, more than 87% of cells from three cell lines (4T1, HeLa, and A549 cells) survived after 24-hr treatment with PSP at a concentration up to 200 μg mL^{-1}. This indicates that PSP NCs are nontoxic to the tested cells. Meanwhile, 5-min NIR irradiation alone (when the concentration of NCs is 0 μg mL^{-1}) has negligible toxicity in 4T1 cells (Figures 4A and 4B), which shows that the slight decrease in cell viability upon treatment by PSP and PSPZP NCs in hypoxic conditions should come from photothermal therapy (PTT) of NCs under NIR irradiation. The 24-hr treatments with PSPZP NCs in normoxic conditions have more cytotoxicity than treatments in hypoxic conditions. To mimic an H_2O_2-rich cancer microenvironment, 100 μM H_2O_2 was added into cell media in hypoxic conditions (Szatrowski and Nathan, 1991). Results show that the introduction of H_2O_2 could greatly increase the cytotoxicity of PSPZP NCs under NIR irradiation, which should result from the increased $^1O_2$ generation because the photothermal conversion of NCs could speed up the H_2O_2 decomposition and O_2 generation. To further demonstrate the catalytic ability of PSP NCs, mesoporous silica NPs were synthesized through an etching process of PB@SiO_2 under alkaline solution (see Transparent Methods). Transmission electron micrographs (Figure S12) show that mesoporous silica without inner PB still maintains its original cubic morphology. Then, ZnPc-loaded mesoporous silica was used to study the O_2-dependent PDT ability under hypoxic condition. Results indicated that without inner PB, H_2O_2 cannot be converted into O_2, and thus the killing efficiency will be suppressed (Figure S13). To further confirm the influence of temperature on PDT efficiency, we performed cell viability test of PSPZP NCs under different incubation temperatures. As shown in Figure 4C, with the increase in incubation temperature from 37°C to 43°C, greater cytotoxicities have been observed. Flow cytometry was used to conduct apoptosis analysis of annexin V-fluorescein isothiocyanate and propidium iodide double-stained 4T1 cells treated in different conditions. As shown in Figure 4D, an obvious increased apoptotic rate (Q2 + Q3) is present with the increase of incubation temperature. All *in vitro* cytotoxic results showed that the local temperature enhanced by the introduction of NIR irradiation plays a key role in increasing the O_2 and $^1O_2$ generation, therefore enhancing the PDT efficiency of PSPZP NCs.

In Vivo Photoacoustic and Positron Emission Tomographic Imaging

As a widely used noninvasive biomedical modality, photoacoustic imaging (PAI) is a newly developed method that employs laser light to acoustically visualize biological tissues (Liba and de La Zerda, 2017). Owing to the strong absorbance in the NIR region, PAI of PSP NCs was assessed *in vitro* and *in vivo*.

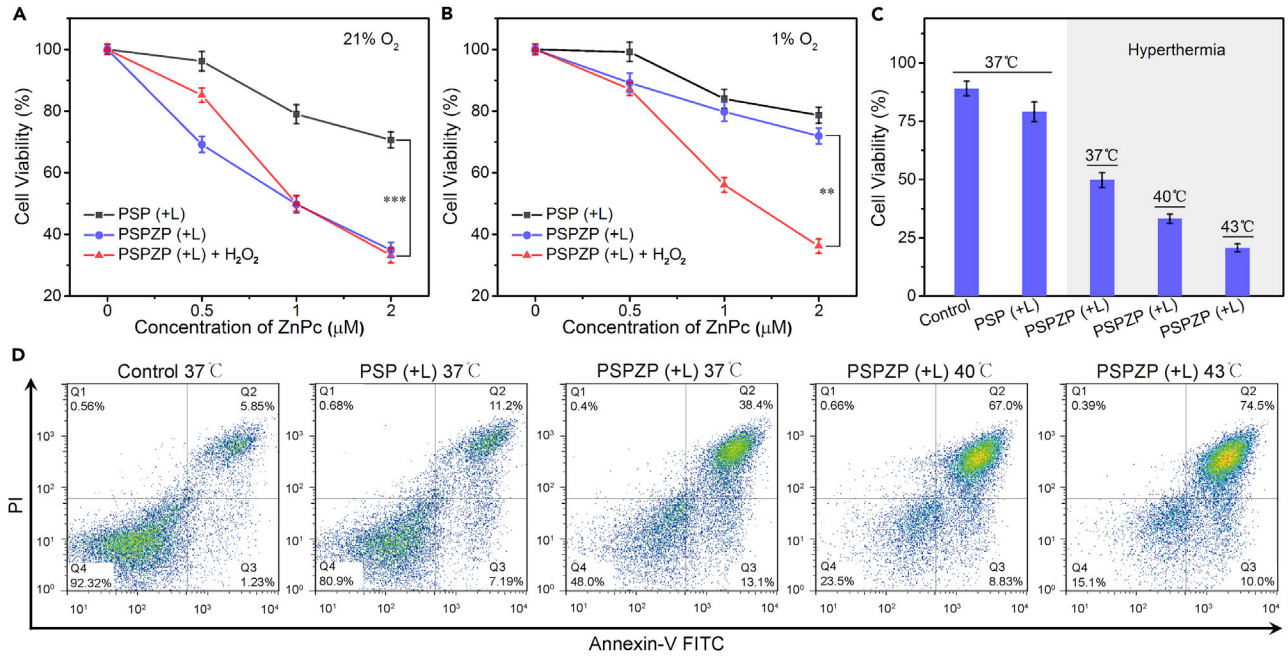

Figure 4. Enhanced Cytotoxicity by PSPZP NCs in Normal and Hypoxic Conditions

(A and B) Viabilities of (A) normoxic and (B) hypoxic 4T1 cells treated with PSP or PSPZP with or without addition of H_2O_2 under NIR irradiation (671 nm, 0.4 W cm^{-2}, 5 min).

(C) Relative viabilities of 4T1 cells incubated with PSP or PSPZP NCs (PSP concentration in both NCs is 50 μg/mL) in normoxic (37°C) and hypoxic (37°C, 40°C, 43°C) environments under NIR irradiation (671 nm, 0.4 W cm^{-2}, 5 min).

(D) Flow cytometry analysis of 4T1 cells after receiving different treatments.

Statistical analysis was performed using the Student's two-tailed test (**$p < 0.01$ and ***$p < 0.001$).

Photoacoustic (PA) signals were first plotted as a function of PSP NCs concentration (Figure S14), which has a linear relationship with a slope of 2.94. 4T1 tumor-bearing mice were selected as model for *in vivo* imaging. PSP NCs were administered through intravenous injection at a dose of 4 mg kg^{-1}, and the excitation wavelength was fixed at 730 nm. Quantitatively, the average PA signal intensity was increased by 225.8% and 244.7% for tumor at 0.5 and 4 hr post-injection respectively, relative to the signal intensities of the tumor before the injection (Figures 5A and S15).

Positron emission tomography (PET) can offer high sensitivity and accurate quantification when compared with other imaging modalities. It has been widely employed in the field of molecular imaging for disease diagnosis, drug tracking, and treatment monitoring (Thakor and Gambhir, 2013). Radionuclide ^{89}Zr has an optimal half-life ($t_{1/2}$ = 78.4 hr) and relatively low positron energy (β^+_{avg} = 395.5 keV), making it suitable for long-term *in vivo* tracking of NPs (Yin et al., 2011). For these reasons, ^{89}Zr-based radiopharmaceuticals are now being actively developed for clinical applications, with at least five clinical trials in the United States alone using ^{89}Zr-labeled antibodies (many more in Europe) (Chen et al., 2015b; Goel et al., 2016). PET imaging was further used to evaluate tumor imaging and biodistribution of PSP NCs *in vivo*. As shown in Figure 5B, $^{89}Zr^{4+}$ could be stably loaded into PSP NCs because the deprotonated silanol groups (-Si-O^-) in mesoporous silica shell could function as hard Lewis acid sites for stable chelator-free radiolabeling of hard Lewis bases. Herein, results revealed that the labeling yields were 84.5% due to the presence of abundant deprotonated silanol groups inside the mesochannels of mesoporous silica (Figure 5C). To ensure the labeling stability of ^{89}Zr, ^{89}Zr-labeled PSP was mixed with mouse serum and shaken at 37°C and 56°C. By measuring the remaining radioactivities in those samples, we found that ^{89}Zr-PSP was highly stable within 24 hr in serum (Figure 5D). The PSP NCs with stable ^{89}Zr loading were then intravenously injected into mice. As shown in Figure 5E, the obvious tumor contrast was observed 6 hr after injection. These imaging results indicate that the PSP NCs could effectively remain in tumor site due to the enhanced permeability and retention effect of cancerous tumors, and therefore have a great potential for *in vivo* imaging-guided cancer therapy (Maeda, 2015; Wang et al., 2018). To further study the biodistribution of PSP NCs *in vivo*, mice treated with ^{89}Zr-PSP NCs were sacrificed 24 hr after injection. The radioactivities in major tissues and

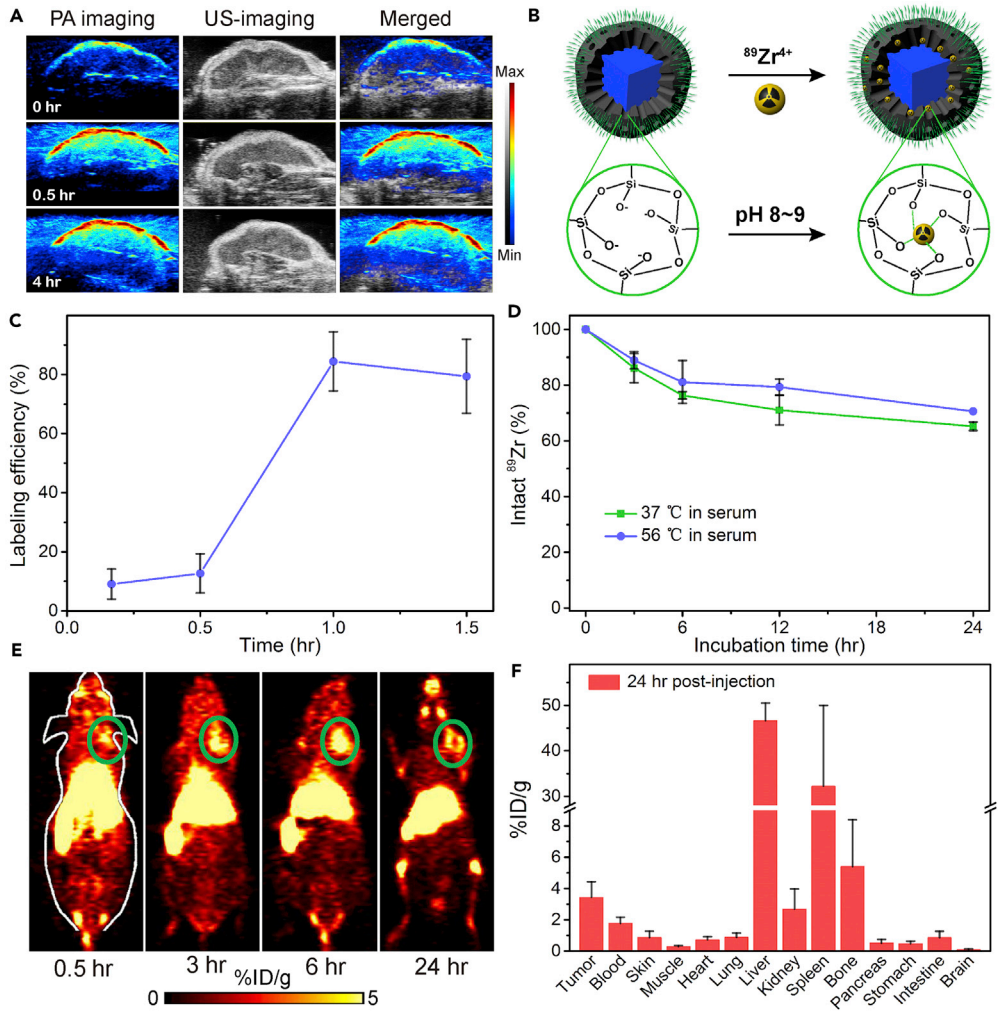

Figure 5. *In Vivo* Photoacoustic and Positron Emission Tomography Imaging of PSP NCs

(A) *In vivo* 2D ultrasonic and PA imaging of 4T1 tumor in mice injected with PSP NCs acquired at 0 hr and after post-injection (0.5 hr and 4 hr).

(B) Schematic illustration showing the labeling of $^{89}Zr^{4+}$ to the deprotonated silanol groups (-Si-O-) from the meso channels.

(C) Quantified labeling yield of ^{89}Zr on PSP NCs at various time points.

(D) Stability test of ^{89}Zr labeling on PSP NCs after incubation in serum at 37°C or 56°C for different periods of time.

(E) PET images of 4T1 tumor-bearing mice taken at various time points (0.5, 3, 6, and 24 hr) after i.v. injection of ^{89}Zr-PSP NCs. The green circles highlight the 4T1 tumor site of mice.

(F) Biodistribution of ^{89}Zr-PSP NCs in different organs at 24 hr after being injected into 4T1 tumor-bearing mice. The unit is the percentage of injected dose per gram of tissue (%ID/g).

Error bars were based on the standard error (mean ± SEM, n = 3).

organs were measured using a γ-counter (Figure 5F). In addition to the tumors, larger radioactivities were noted in the liver and spleen, which result from the clearance of foreign NPs by macrophage uptake (Liu et al., 2015; Moghimi and Hunter, 2001).

In Vivo PDT and PTT Using Intravenous Injection

To examine the photo-enhanced therapeutic efficacy of PSPZP NCs on treating tumors *in vivo*, mice bearing 4T1 tumor were administered NCs by intravenous injection, and tumors were then subjected or not subjected to NIR irradiation (671 nm, 0.4 W cm^{-2}) for 5 min at 24 hr post-injection. Tumor-bearing mice were randomly divided into 6 groups with six mice per group. As shown in Figure 6A, mice injected

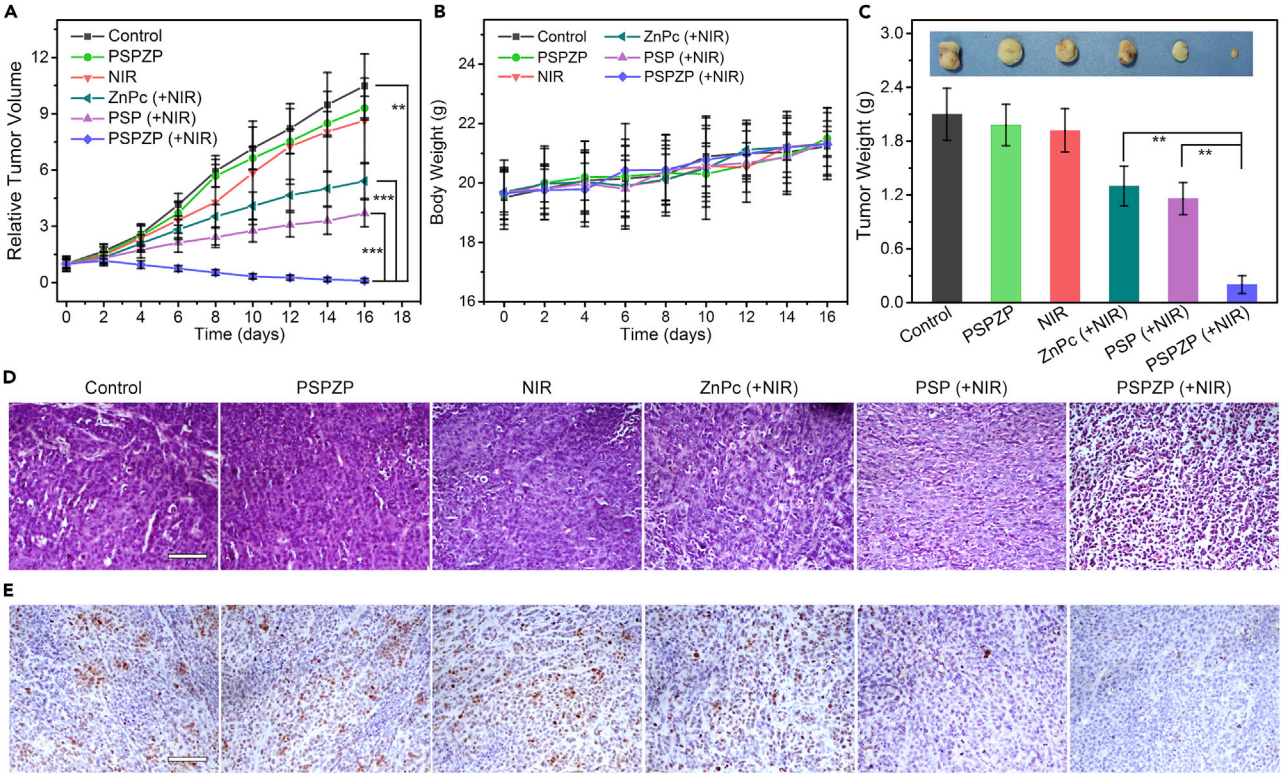

Figure 6. *In Vivo* PDT and PTT Using Intravenous Injection in a Subcutaneous Tumor Model

(A) Relative tumor volume variation of mice treated under different conditions (n = 6).

(B) Average body weights of mice that received different treatments.

(C) Average weights and typical photographs (inset) of tumors collected from mice at the end of treatments (day 16).

(D) Slices of tumor tissues stained with H&E after different treatments. Scale bar, 50 μm.

(E) Optical microscopic images of tumor sections stained by Ki-67 from different groups. Scale bar, 50 μm.

Statistical analysis was performed using the Student's two-tailed t test (**$p < 0.01$ and ***$p < 0.001$).

with saline (control) and PSPZP demonstrated the greatest tumor growth. Similarly, NIR irradiation alone has no influence on tumor growth.

However, tumors in mice treated with ZnPc plus NIR and PSP plus NIR showed obvious reduced growth due to the PDT of ZnPc and PTT of PSP under NIR irradiation, respectively. Notably, a significant tumor inhibition was observed in mice treated with PSPZP plus NIR irradiation. After one round of this treatment, the tumors exhibited no further growth. In addition, mice in all treated groups showed a similar body increase tendency and did not show apparent weight loss (Figure 6B). At day 16, tumors from all groups were harvested and weighed (Figure 6C). The tumor weight in saline-, PSPZP-, or NIR-treated mice is larger than that of mice treated with ZnPc + NIR (PDT) or PSP + NIR (PTT). Importantly, compared with PDT or PTT treatment, the therapeutic efficacy achieved by the combinatory therapy (PSPZP + NIR) appeared to be much higher than the additive efficacy of PDT and PTT used alone based on the tumor growth reduction ratio at day 16, suggesting a synergistic effect of the combinatory therapy. As revealed by micrographs of an H&E-stained tumor slice, prominent cell damage was found in the tumor treated with PSPZP + NIR (Figure 6D). Besides, cancer cells show a higher suppressed proliferation in the PSPZP + NIR group as shown in the Ki-67 staining when compared with other groups (Figure 6E), further indicating the enhanced PDT efficacy. Based on the above results, the PSPZPs NCs demonstrated great potential as an excellent nanoplatform for enhanced PDT due to the photo-enhanced endogenous O_2 generation for relieving tumor hypoxia.

In Vivo Anti-tumor Mechanism and Long-Term Biocompatibility Test

To investigate the ability of NCs to relieve tumor hypoxia *in situ* for cancer therapy, a hypoxyprobe (pimonidazole) immunofluorescence assay was carried out on tumor slices extracted from mice treated with PSP

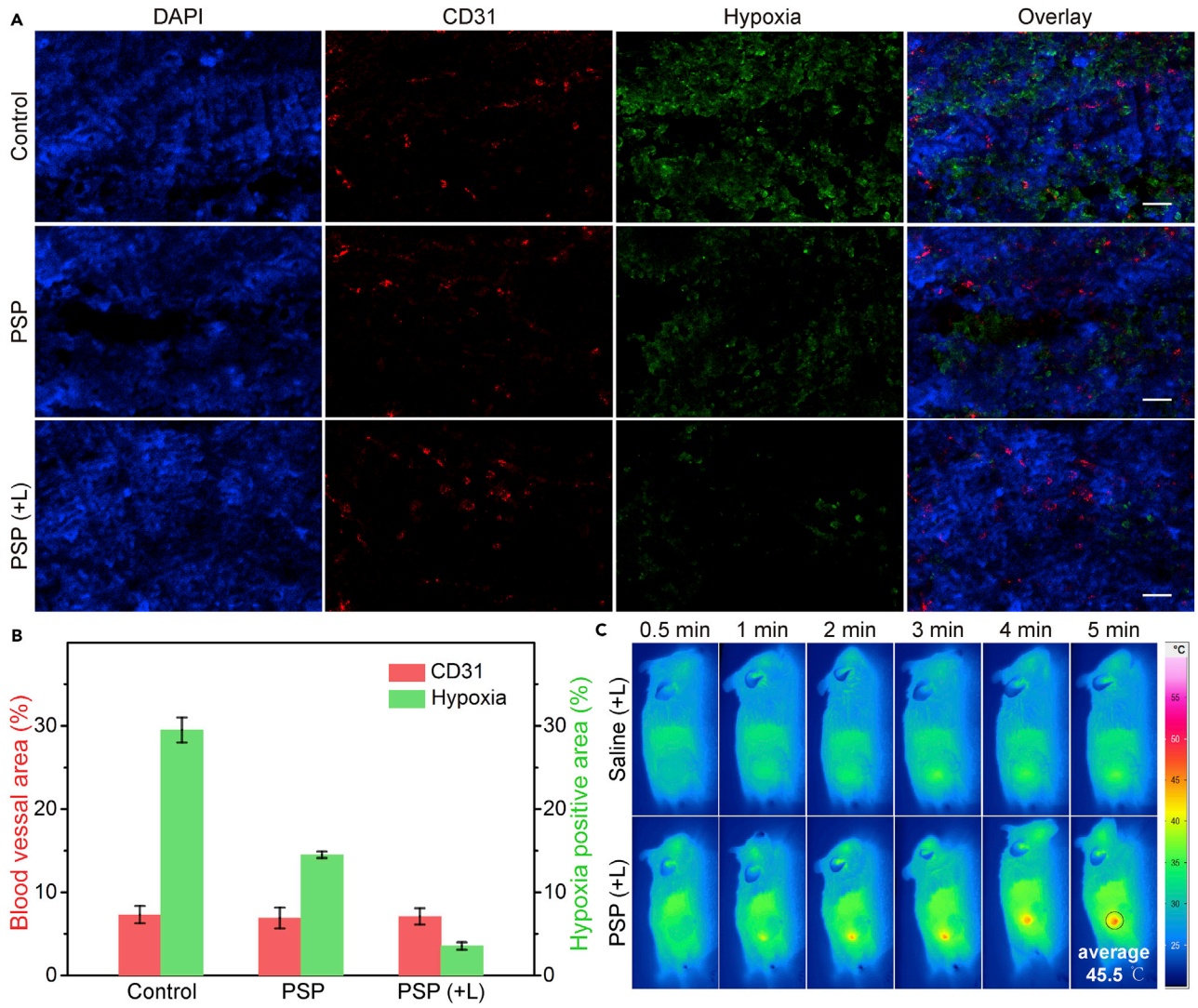

Figure 7. *In Vivo* Anti-tumor Mechanism of PDT and PTT

(A) Representative immunofluorescence images of tumor slices after hypoxia staining. The hypoxia areas and blood vessels were stained by anti-pimonidazole antibody (green) and anti-CD31 antibody (red), respectively. Scale bar, 50 μm.

(B) The relative hypoxia-positive areas and blood vessel densities as recorded from nine images using the ImageJ software.

(C) Full-body thermographic images of 4T1-tumor-bearing mice treated with saline and PSP NCs within 5-min NIR irradiation.

NCs for 24 hr. Anti-mouse CD31 antibody was used to locate blood vessels inside the tumor. Compared with the control group, the tumor slices from mice treated with PSP NCs showed obviously reduced green fluorescence (pimonidazole-stained hypoxia), indicating that the tumor hypoxia was relieved (Figure 7A). Semi-quantitative statistical analysis of hypoxia-positive areas and blood vessel densities based on nine confocal images further indicated that the PSP NCs, especially with the assistance of NIR irradiation, could greatly reduce tumor hypoxia without affecting blood vessel densities (Figure 7B). Moreover, a significant decrease of green fluorescence was observed in the group treated with PSP NCs plus NIR irradiation. Such photo-enhanced hypoxia improvement should come from the *in situ* increased endogenous H_2O_2 decomposition and O_2 generation due to the NIR-enhanced local temperature enhancement (Figure 7C). Furthermore, to validate the delivery of PSP NCs to the interior of tumor, *in vivo* magnetic resonance (MR) imaging was performed as it can provide exquisite anatomical images with high spatial resolution without the restriction of imaging depth (Smith and Gambhir, 2017; Wang et al., 2016). Upon intravenous injection of PSP NCs (20 mg/kg), T1-weighted MR signals gradually lighted up, whereas

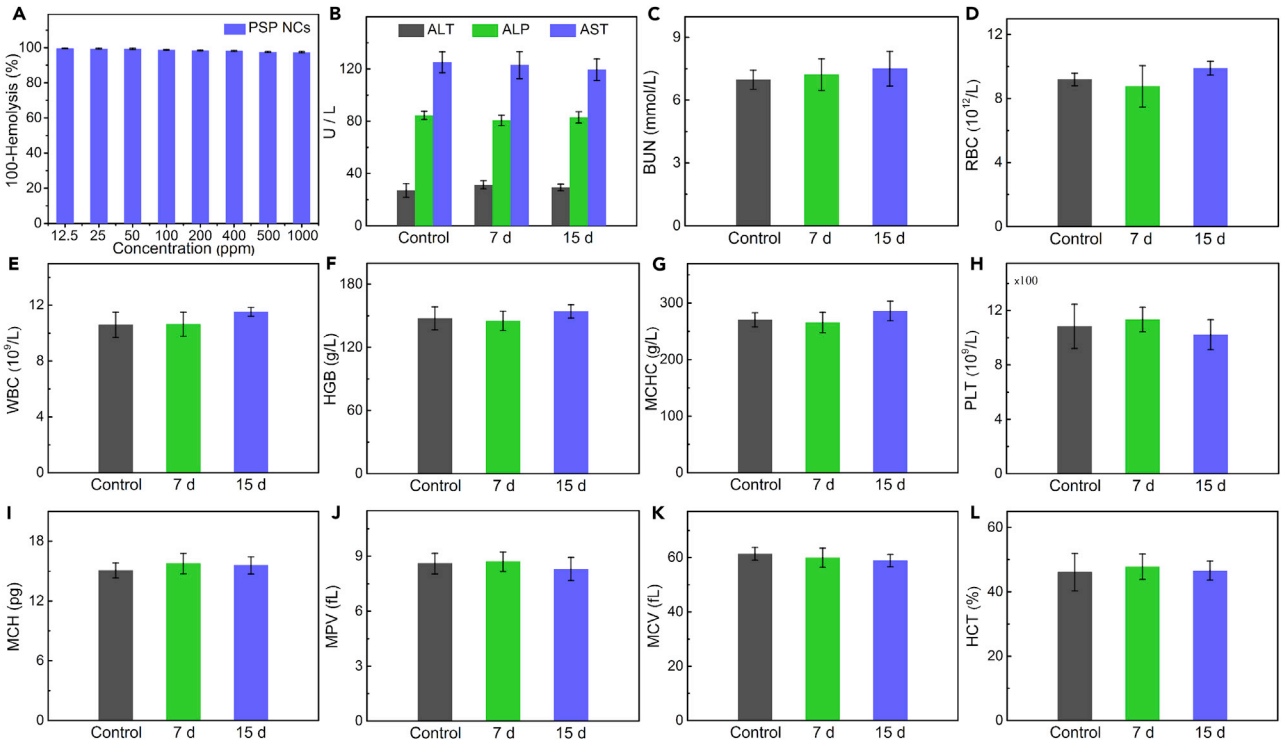

Figure 8. Long-Term Biocompatibility Test

(A) Hemolysis of PSPZP NCs at various concentrations.

(B) The levels of alanine transaminase (ALT), alkaline phosphatase (ALP), and aspartate aminotransferase (AST) of untreated mice (control) and PSPZP NC-injected mice at 7 and 15 days.

(C) The level of blood urea nitrogen (BUN) of untreated mice (control) and PSPZP NC-injected mice at 7 and 15 days.

(D–L) Hematology data of red blood cell (RBC) (D), white blood cell (WBC) (E), hemoglobin (HGB) (F), mean corpuscular hemoglobin concentration (MCHC) (G), platelet (PLT) (H), mean corpuscular hemoglobin (MCH) (I), mean platelet volume (MPV) (J), mean corpuscular volume (MCV) (K), and hematocrit (HCT) (L) in the untreated mice (control) and in mice treated with the PSPZP NCs. Error bars were based on the standard error (mean ± SEM, n = 3).

T2-weighted MR signals decreased in the interior region of tumor sites 24 hr later (Figure S16), indicating that PSP NCs have been delivered to the interior of the tumor, which is considered to be hypoxia (Wilson and Hay, 2011).

The hemolysis of PSPZP NCs was studied to test their safety *in vivo*. As shown in Figure 8A, no visible hemolytic effects (<3%) were observed even at a PSP concentration up to 1,000 μg mL^{-1}. The long-term toxicity of PSPZP NCs on healthy tissues was also investigated via *in vivo* blood biochemistry test, blood routine analysis, and H&E staining. The blood of healthy BALB/c mice was drawn from the tail artery at different time points (7 and 15 days) after intravenous injection of PSPZP NCs, whereas an untreated group was used as the control. For blood biochemistry test, alanine transaminase, alkaline phosphatase, aspartate aminotransferase, and blood urea nitrogen served as hepatic and renal function markers. As shown in Figures 8B and 8C, no significant changes were observed between control, 7 days, and 15 days, indicating the good hepatic and renal safety property of PSPZP NCs. For blood routine analysis, parameters such as red blood cells, white blood cell, hemoglobin, mean corpuscular hemoglobin concentration, platelets, mean corpuscular hemoglobin, mean platelet volume, mean corpuscular volume, and hematocrit were measured (Figures 8D–8L). All the nine markers are well within the normal ranges, suggesting the negligible *in vivo* toxicity of PSPZP at the treatment dose within 15 days (Liu et al., 2016). The potential toxicity of nanoscale therapeutic agent has been a major safety concern for clinical applications. To test the biocompatibility of the NCs *in vivo*, we performed histological analysis on various tissues (heart, kidney, liver, lung, and spleen) from mice injected with PBS, PB NPs, $mSiO_2$, PSP NCs, and PSPZP NCs to identify signs of acute toxicity. Tissues were harvested from mice 120 hr after NC injection, fixed in 10% formalin, embedded in paraffin, sectioned, and stained with H&E. As shown in Figure 9, no obvious tissue damage or inflammatory

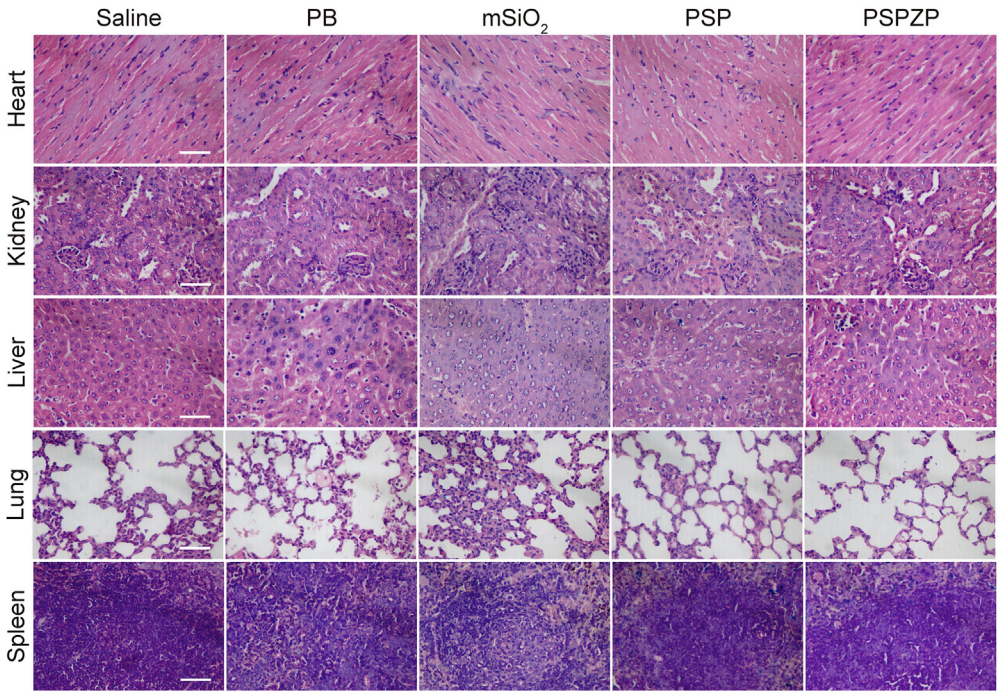

Figure 9. H&E Staining

H&E-stained tissue sections of mouse heart, kidney, liver, lung, and spleen obtained from saline-injected animals, and those injected with PB NPs, $mSiO_2$, PSP NCs, and PSPZP NCs. Scale bar, 50 μm.

lesion in these main organs was observed, which indicates that all samples have no obvious damage in normal tissues. Thanks to the FDA-approved compositions in the nanostructure, the reported NCs herein are nontoxic and safe and suitable for biomedical applications.

DISCUSSION

In summary, multifunctional and safe PSP NCs have been successfully synthesized by the surface coating of biocompatible PB NPs with mesoporous silica shell modified with PEG chains. Combining each function of building blocks, the as-synthesized PSP NCs not only maintain the properties of the individual constituents but also display cooperative properties for photo-enhanced H_2O_2 decomposition and O_2 generation. *In vitro* and *in vivo* results show that the single laser-induced $^1O_2$ generation could *in situ* relieve cancer hypoxia for enhanced cancer therapy by combined photothermal therapy/PDT. The NIR absorption and the ^{89}Zr loading of PSP endow NCs the dual-modal PET and PAI imaging function to identify the tumor location and monitor the treatment progress. Such designed NCs demonstrate great promise toward advanced nanoplatforms for simultaneous imaging diagnostics and high-efficacy therapy.

Limitations of Study

This work proposes a new possibility to construct multifunctional system through photo-induced local temperature enhancement for modulating catalytic reaction toward tumor-overexpressed hydrogen peroxide for augmented PDT. Although demonstrated experimentally, the low tumor accumulation and lack of targeting agent limit the further optimization of treatment efficiency for such a multifunctional system.

METHODS

All methods can be found in the accompanying Transparent Methods supplemental file.

SUPPLEMENTAL INFORMATION

Supplemental Information includes Transparent Methods and 16 figures and can be found with this article online at https://doi.org/10.1016/j.isci.2018.10.005.

ACKNOWLEDGMENTS

This work was supported by the MOST Grant 2016YFA0101202; The National Natural Science Foundation of China, 21571168, 31471268, and U1232211; National Key R&D Program of China 2016YFA0401801; Innovative Program of Development Foundation of Hefei Center for Physical Science and Technology (2016FXCX005); CAS/SAFEA International Partnership Program for Creative Research Teams and CAS Hefei Science Center (2016HSC-IU011); the NIH (P30CA014520); and the American Cancer Society (125246-RSG-13-099-01-CCE). The authors are also thankful for the support of the Core Facility Center for Life Sciences of University of Science and Technology of China for imaging support.

AUTHOR CONTRIBUTIONS

Conceptualization, Q.C., W.C. and Z.G.; Methodology, D.W., R.S., H.Wang and G.X.; Investigation, D.W., R.S. and P.X.; Experiments, D.W., R.S., J.Z., S.S. and H.Wu; Writing – Original Draft, D.W. and R.S.; Writing – Review & Editing, D.W. and H.Wang; Funding Acquisition, Q.C., Z.G., and W.C.; Resources, Q.C., W.C., Z.G. and T.E.B.; Supervision, Q.C., Z.G., and W.C.; D.W., R.S. and J.Z. conducted the project and contributed equally. Dedicated to University of Science and Technology of China (USTC) on the occasion of its 60th anniversary.

DECLARATION OF INTERESTS

The authors declare no competing interest.

Received: July 31, 2018
Revised: September 20, 2018
Accepted: October 8, 2018
Published: November 30, 2018

REFERENCES

Abbas, M., Zou, Q., Li, S., and Yan, X. (2017). Self-assembled peptide- and protein-based nanomaterials for antitumor photodynamic and photothermal therapy. Adv. Mater. *29*, 1605021.

Bristow, R.G., and Hill, R.P. (2008). Hypoxia, DNA repair and genetic instability. Nat. Rev. Cancer *8*, 180.

Brohi, R.D., Wang, L., Talpur, H.S., Wu, D., Khan, F.A., Bhattarai, D., Rehman, Z.U., Farmanullah, F., and Huo, L.J. (2017). Toxicity of nanoparticles on the reproductive system in animal models: a review. Front. Pharmacol. *8*, 00606.

Brown, S.B., Brown, E.A., and Walker, I. (2004). The present and future role of photodynamic therapy in cancer treatment. Lancet Oncol. *5*, 497–508.

Calixto, G., Bernegossi, J., Freitas, L., Fontana, C., and Chorilli, M. (2016). Nanotechnology-based drug delivery systems for photodynamic therapy of cancer: a review. Molecules *21*, 342.

Chen, H., Tian, J., He, W., and Guo, Z. (2015a). H_2O_2-activatable and O_2-evolving nanoparticles for highly efficient and selective photodynamic therapy against hypoxic tumor cells. J. Am. Chem. Soc. *137*, 1539–1547.

Chen, F., Goel, S., Valdovinos, H.F., Luo, H., Hernandez, R., Barnhart, T.E., and Cai, W. (2015b). In vivo integrity and biological fate of chelator-free zirconium-89-labeled mesoporous silica nanoparticles. ACS Nano *9*, 7950–7959.

Chen, J., Luo, H., Liu, Y., Zhang, W., Li, H., Luo, T., Zhang, K., Zhao, Y., and Liu, J. (2017). Oxygen-self-produced nanoplatform for relieving hypoxia and breaking resistance to sonodynamic treatment of pancreatic cancer. ACS Nano *11*, 12849–12862.

Cheng, L., Gong, H., Zhu, W., Liu, J., Wang, X., Liu, G., and Liu, Z. (2014). PEGylated Prussian blue nanocubes as a theranostic agent for simultaneous cancer imaging and photothermal therapy. Biomaterials *35*, 9844–9852.

Cheng, Y., Cheng, H., Jiang, C., Qiu, X., Wang, K., Huan, W., Yuan, A., Wu, J., and Hu, Y. (2015). Perfluorocarbon nanoparticles enhance reactive oxygen levels and tumour growth inhibition in photodynamic therapy. Nat. Commun. *6*, 8785.

Cheng, H., Zhu, J.Y., Li, S.Y., Zeng, J.Y., Lei, Q., Chen, K.W., Zhang, C., and Zhang, X.Z. (2016). An O_2 self-sufficient biomimetic nanoplatform for highly specific and efficient photodynamic therapy. Adv. Funct. Mater. *26*, 7847–7860.

Dolmans, D.E., Fukumura, D., and Jain, R.K. (2003). Photodynamic therapy for cancer. Nat. Rev. Cancer *3*, 380.

Dougherty, T.J., Gomer, C.J., Henderson, B.W., Jori, G., Kessel, D., Korbelik, M., Moan, J., and Peng, Q. (1998). Photodynamic therapy. J. Natl. Cancer Inst. *90*, 889–905.

Fan, W., Bu, W., Shen, B., He, Q., Cui, Z., Liu, Y., Zheng, X., Zhao, K., and Shi, J. (2015). Intelligent MnO_2 nanosheets anchored with upconversion nanoprobes for concurrent pH-/H_2O_2-responsive UCL imaging and oxygen-elevated synergetic therapy. Adv. Mater. *27*, 4155–4161.

Ge, J., Lan, M., Zhou, B., Liu, W., Guo, L., Wang, H., Jia, Q., Niu, G., Huang, X., Zhou, H., et al. (2014). A graphene quantum dot photodynamic therapy agent with high singlet oxygen generation. Nat. Commun. *5*, 4596.

Goel, S., Chen, F., Luan, S., Valdovinos, H.F., Shi, S., Graves, S.A., Ai, F., Barnhart, T.E., Theuer, C.P., and Cai, W. (2016). Engineering intrinsically zirconium-89 radiolabeled self-destructing mesoporous silica nanostructures for in vivo biodistribution and tumor targeting studies. Adv. Sci. *3*, 1600122.

Hopper, C. (2000). Photodynamic therapy: a clinical reality in the treatment of cancer. Lancet Oncol. *1*, 212–219.

Huang, P., Lin, J., Wang, X., Wang, Z., Zhang, C., He, M., Wang, K., Chen, F., Li, Z., Shen, G., et al. (2012). Light-triggered theranostics based on photosensitizer-conjugated carbon dots for simultaneous enhanced-fluorescence imaging and photodynamic therapy. Adv. Mater. *24*, 5104–5110.

Huang, C.C., Chia, W.T., Chung, M.F., Lin, K.J., Hsiao, C.W., Jin, C., Lim, W.H., Chen, C.C., and Sung, H.W. (2016). An implantable depot that can generate oxygen in situ for overcoming hypoxia-induced resistance to anticancer drugs in chemotherapy. J. Am. Chem. Soc. *138*, 5222–5225.

Jia, Q., Ge, J., Liu, W., Zheng, X., Chen, S., Wen, Y., Zhang, H., and Wang, P. (2018). A Magnetofluorescent carbon dot assembly as an acidic H_2O_2-driven oxygenerator to regulate tumor hypoxia for simultaneous bimodal imaging and enhanced photodynamic therapy. Adv. Mater. *30*, 6069.

Jin, C.S., Lovell, J.F., Chen, J., and Zheng, G. (2013). Ablation of hypoxic tumors with dose-equivalent photothermal, but not photodynamic, therapy using a nanostructured porphyrin assembly. ACS Nano *7*, 2541–2550.

Juarranz, Á., Jaén, P., Sanz-Rodríguez, F., Cuevas, J., and González, S. (2008). Photodynamic therapy of cancer. basic principles and applications. Clin. Transl. Oncol. *10*, 148–154.

Kuang, Y., Balakrishnan, K., Gandhi, V., and Peng, X. (2011). Hydrogen peroxide inducible DNA cross-linking agents: targeted anticancer prodrugs. J. Am. Chem. Soc. *133*, 19278–19281.

Liba, O., and de La Zerda, A. (2017). Photoacoustic tomography: breathtaking whole-body imaging. Nat. Biomed. Eng. *1*, 0075.

Lin, J., Wang, S.J., Huang, P., Wang, Z., Chen, S.H., Niu, G., Li, W.W., He, J., Cui, D.X., Lu, G.M., et al. (2013). Photosensitizer-loaded gold vesicles with strong plasmonic coupling effect for imaging-guided photothermal/photodynamic therapy. ACS Nano *7*, 5320–5329.

Liu, T., Shi, S., Liang, C., Shen, S., Cheng, L., Wang, C., Song, X., Goel, S., Barnhart, T.E., Cai, W., and Liu, Z. (2015). Iron oxide decorated MoS_2 nanosheets with double PEGylation for chelator-free radiolabeling and multimodal imaging guided photothermal therapy. ACS Nano *9*, 950–960.

Liu, J., Yang, Y., Zhu, W., Yi, X., Dong, Z., Xu, X., Chen, M., Yang, K., Lu, G., Jiang, L., and Liu, Z. (2016). Nanoscale metal-organic frameworks for combined photodynamic & radiation therapy in cancer treatment. Biomaterials *97*, 1–9.

Lucky, S.S., Soo, K.C., and Zhang, Y. (2015). Nanoparticles in photodynamic therapy. Chem. Rev. *115*, 1990–2042.

Maeda, H. (2015). Toward a full understanding of the EPR effect in primary and metastatic tumors as well as issues related to its heterogeneity. Adv. Drug Deliv. Rev. *91*, 3–6.

Mitchell, J.B., McPherson, S., DeGraff, W., Gamson, J., Zabell, A., and Russo, A. (1985). Oxygen dependence of hematoporphyrin derivative-induced photoinactivation of Chinese hamster cells. Cancer Res. *45*, 2008–2011.

Moghimi, S.M., and Hunter, C. (2001). Capture of stealth nanoparticles by the body's defences. Crit. Rev. Ther. Drug Carrier Syst. *18*, 527–550.

Mou, J., Lin, T., Huang, F., Chen, H., and Shi, J. (2016). Black titania-based theranostic nanoplatform for single NIR laser induced dual-modal imaging-guided PTT/PDT. Biomaterials *84*, 13–24.

Noh, I., Lee, D., Kim, H., Jeong, C.U., Lee, Y., Ahn, J.O., Hyun, H., Park, J.H., and Kim, Y.C. (2018). Enhanced photodynamic cancer treatment by mitochondria-targeting and brominated near-infrared fluorophores. Adv. Sci. *5*, 1700481.

Romero-Castillo, L., Posadas, I., and Ceña, V. (2017). Exploring the in vivo toxicity of nanoparticles. Can. J. Chem. *95*, 917–926.

See, K.L., Forbes, I.J., and Betts, W.H. (1984). Oxygen dependency of photocytotoxicity with haematoporphyrin derivative. Photochem. Photobiol. *39*, 631–634.

Smith, B.R., and Gambhir, S.S. (2017). Nanomaterials for in vivo imaging. Chem. Rev. *117*, 901–986.

Srivastava, V., Gusain, D., and Sharma, Y.C. (2015). Critical review on the toxicity of some widely used engineered nanoparticles. Ind. Eng. Chem. Res. *54*, 6209–6233.

Straten, V.D., Mashayekhi, V., Bruijn, H., Oliveira, S., and Robinson, D. (2017). Oncologic photodynamic therapy: basic principles, current clinical status and future directions. Cancers (Basel) *9*, 19.

Su, Y., Teng, Z., Yao, H., Wang, S., Tian, Y., Zhang, Y., Liu, W., Tian, W., Zheng, L., Lu, N., et al. (2016). A multifunctional PB@mSiO2-PEG/DOX nanoplatform for combined photothermal-chemotherapy of tumor. ACS Appl. Mater. Interfaces *8*, 17038–17046.

Szatrowski, T.P., and Nathan, C.F. (1991). Production of large amounts of hydrogen peroxide by human tumor cells. Cancer Res. *51*, 794–798.

Thakor, A.S., and Gambhir, S.S. (2013). Nanooncology: the future of cancer diagnosis and therapy. CA Cancer J. Clin. *63*, 395–418.

Tian, B., Wang, C., Zhang, S., Feng, L., and Liu, Z. (2011). Photothermally enhanced photodynamic therapy delivered by nano-graphene oxide. ACS Nano *5*, 7000–7009.

Tian, W., Su, Y., Tian, Y., Wang, S., Su, X., Liu, Y., Zhang, Y., Tang, Y., Ni, Q., Liu, W., et al. (2017). Periodic mesoporous organosilica coated prussian blue for MR/PA dual-modal imaging-guided photothermal-chemotherapy of triple negative breast cancer. Adv. Sci. *4*, 1600356.

Triesscheijn, M., Baas, P., Schellens, J., and Stewart, F.A. (2006). Photodynamic therapy in oncology. Oncologist *11*, 1034–1044.

Vander Heiden, M.G., Cantley, L.C., and Thompson, C.B. (2009). Understanding the Warburg effect: the metabolic requirements of cell proliferation. Science *324*, 1029–1033.

Wang, D., Guo, Z., Zhou, J., Chen, J., Zhao, G., Chen, R., He, M., Liu, Z., Wang, H., and Chen, Q. (2015). Novel $Mn_3[Co(CN)_6]_2$@SiO_2@Ag Core-shell nanocube: enhanced two-photon fluorescence and magnetic resonance dual-modal imaging-guided photothermal and chemo-therapy. Small *11*, 5956–5967.

Wang, D., Zhou, J., Chen, R., Shi, R., Zhao, G., Xia, G., Li, R., Liu, Z., Tian, J., Wang, H., et al. (2016). Controllable synthesis of dual-MOFs nanostructures for pH-responsive artemisinin delivery, magnetic resonance and optical dual-model imaging-guided chemo/photothermal combinational cancer therapy. Biomaterials *100*, 27–40.

Wang, D., Wu, H., Zhou, J., Xu, P., Wang, C., Shi, R., Wang, H., Wang, H., Guo, Z., and Chen, Q. (2018). In situ one-pot synthesis of MOF-polydopamine hybrid nanogels with enhanced photothermal effect for targeted cancer therapy. Adv. Sci. *5*, 1800287.

Wilson, W.R., and Hay, M.P. (2011). Targeting hypoxia in cancer therapy. Nat. Rev. Cancer *11*, 393–410.

Xu, R., Wang, Y., Duan, X., Lu, K., Micheroni, D., Hu, A., and Lin, W. (2016). Nanoscale metal-organic frameworks for ratiometric oxygen sensing in live cells. J. Am. Chem. Soc. *138*, 2158–2161.

Yang, F., Hu, S., Zhang, Y., Cai, X., Huang, Y., Wang, F., Wen, S., Teng, G., and Gu, N. (2012). A hydrogen peroxide-responsive O(2) nanogenerator for ultrasound and magnetic-resonance dual modality imaging. Adv. Mater. *24*, 5205–5211.

Yang, G., Xu, L., Chao, Y., Xu, J., Sun, X., Wu, Y., Peng, R., and Liu, Z. (2017). Hollow MnO_2 as a tumor-microenvironment-responsive biodegradable nano-platform for combination therapy favoring antitumor immune responses. Nat. Commun. *8*, 902.

Yang, Z.L., Tian, W., Wang, Q., Zhao, Y., Zhang, Y.L., Tian, Y., Tang, Y.X., Wang, S.J., Liu, Y., Ni, Q.Q., et al. (2018). Oxygen-evolving mesoporous organosilica coated prussian blue nanoplatform for highly efficient photodynamic therapy of tumors. Adv. Sci. (Weinh) *5*, 1700847.

Yin, Z., Hao, H., and Cai, W. (2011). PET tracers based on zirconium-89. Curr. Radiopharm. *4*, 131–139.

Zhang, M., Murakami, T., Ajima, K., Tsuchida, K., Sandanayaka, A.S., Ito, O., Iijima, S., and Yudasaka, M. (2008). Fabrication of ZnPc/protein nanohorns for double photodynamic and hyperthermic cancer phototherapy. Proc. Natl. Acad. Sci. U S A *105*, 14773–14778.

Zhang, C., Zhao, K., Bu, W., Ni, D., Liu, Y., Feng, J., and Shi, J. (2015). Marriage of scintillator and semiconductor for synchronous radiotherapy and deep photodynamic therapy with diminished oxygen dependence. Angew. Chem. Int. Ed. *54*, 1770–1774.

Zheng, D.W., Li, B., Li, C.X., Fan, J.X., Lei, Q., Li, C., Xu, Z., and Zhang, X.Z. (2016). Carbon-dot-decorated carbon nitride nanoparticles for enhanced photodynamic therapy against hypoxic tumor via water splitting. ACS Nano *10*, 8715–8722.

ISCI, Volume *9*

Supplemental Information

Photo-Enhanced Singlet Oxygen Generation of Prussian Blue-Based Nanocatalyst for Augmented Photodynamic Therapy

Dongdong Wang, Ruohong Shi, Jiajia Zhou, Sixiang Shi, Huihui Wu, Pengping Xu, Hui Wang, Guoliang Xia, Todd E. Barnhart, Weibo Cai, Zhen Guo, and Qianwang Chen

Supplemental Data Items

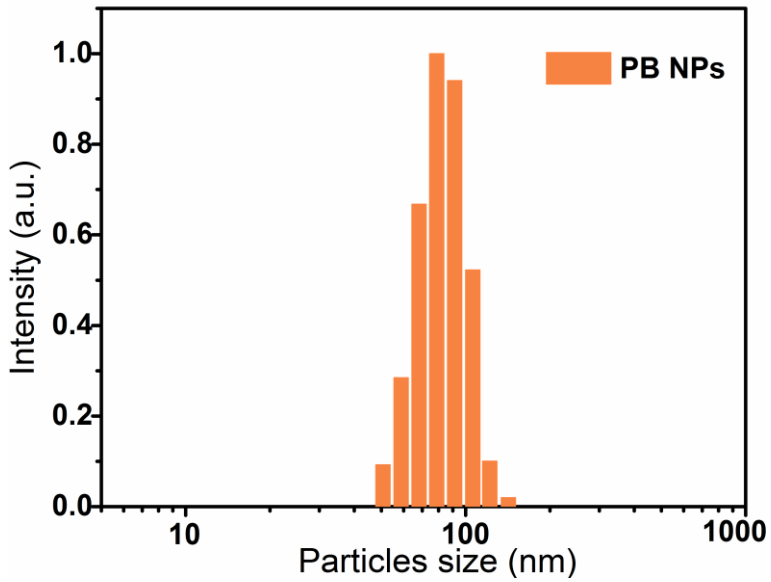

Figure S1. Dynamic light scattering (DLS) size distribution of Prussian Blue (PB) NPs, related to Figure 1.

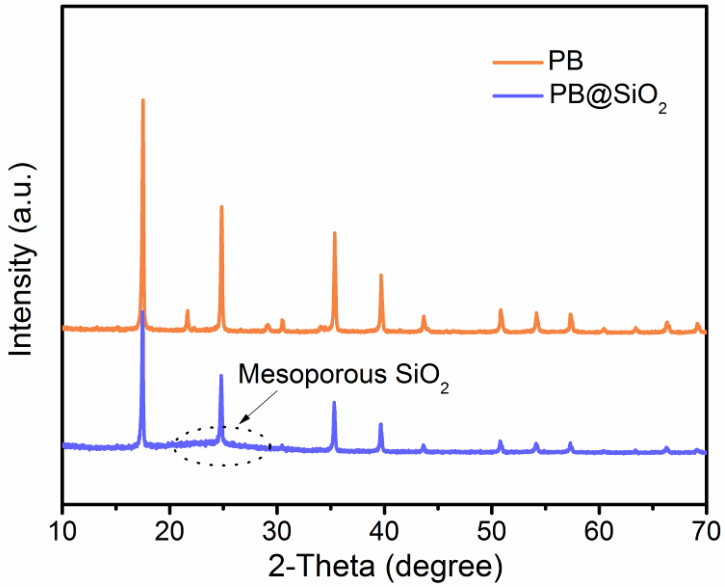

Figure S2. Powder X-ray diffraction (PXRD) pattern of PB and PB@SiO_2 NPs, related to Figure 1.

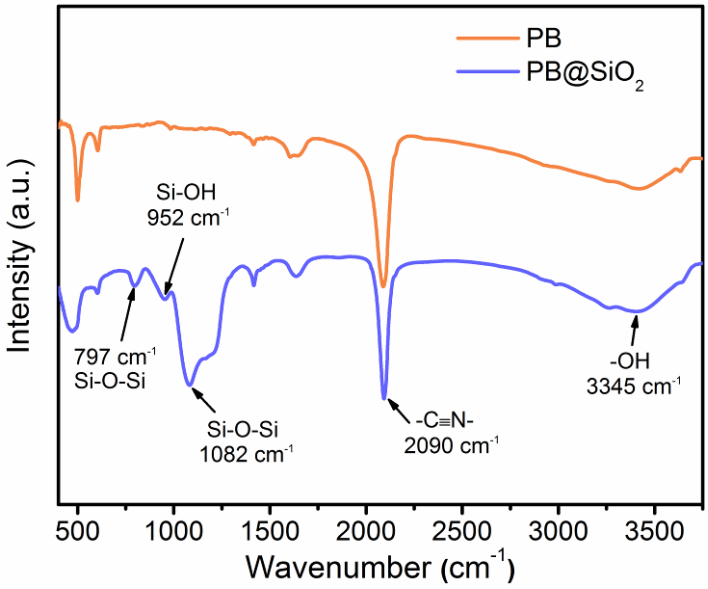

Figure S3. FT-IR spectra of PB and PB@SiO_2 NPs, related to Figure 1.

In the FT-IR spectra (Figure S3), a broad band around 3345 cm^{-1} is due to the -OH stretching and bending vibrations of water. After further mesoporous SiO_2 coating, several broad absorptions assigned to asymmetric stretching (1082 cm^{-1}) and symmetric vibration (797 cm^{-1}) of Si-O-Si and Si-OH (952 cm^{-1}) show the generation of $mSiO_2$ due to the hydrolysis of TEOS. A sharp peak centered at 2090 cm^{-1} should be assign to -C≡N- of PB NPs.

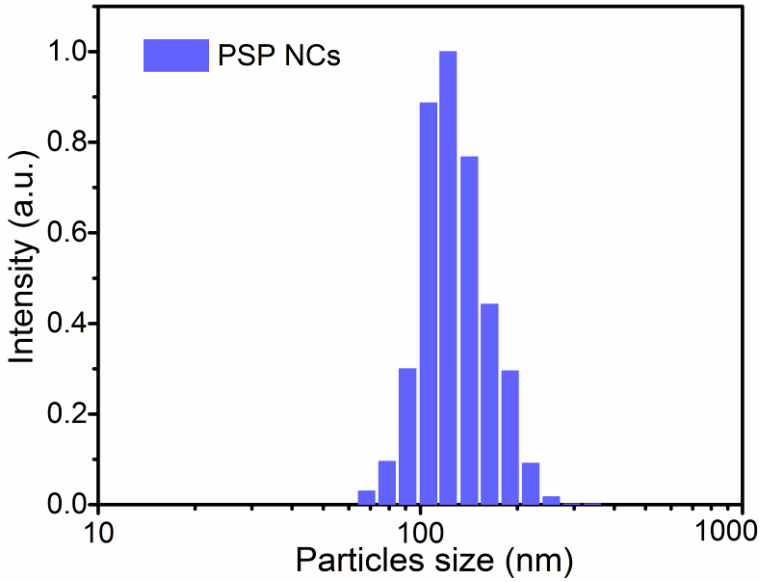

Figure S4. Dynamic light scattering (DLS) size distribution of final PSP NCs, related to Figure 1.

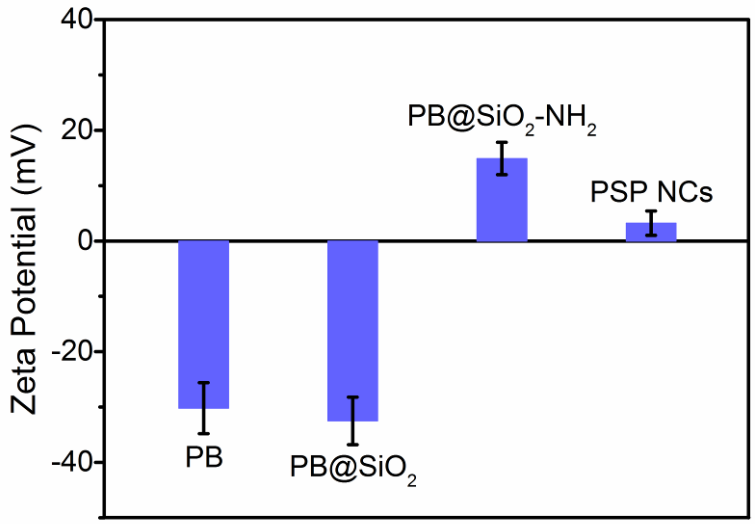

Figure S5. Zeta potential of PB, PB@SiO_2, PB@SiO_2-NH_2 NPs and final PSP NCs, related to Figure 1.

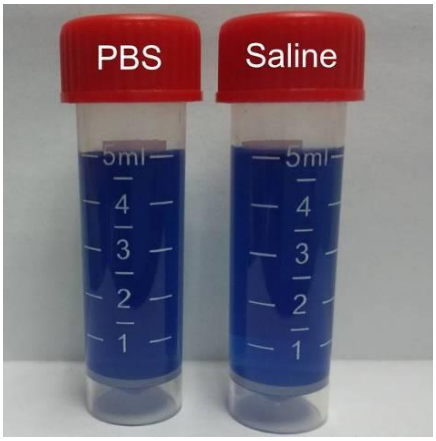

Figure S6. Photos of PSP NCs twenty months after dispersing in PBS and Saline solutions, related to Figure 1.

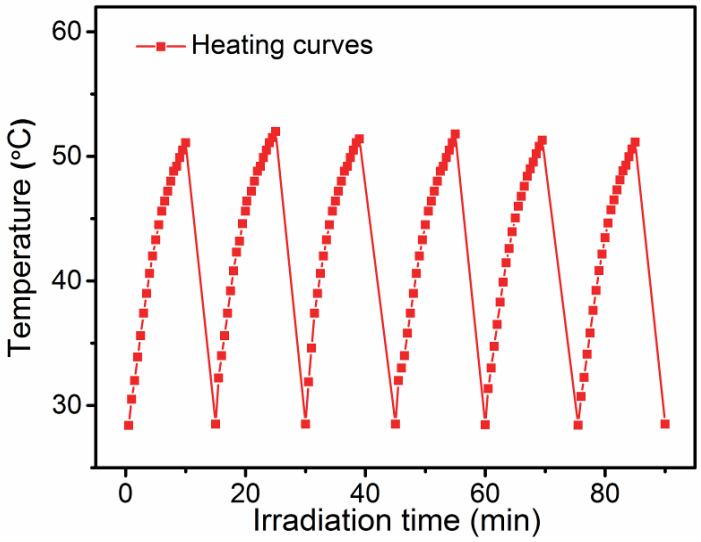

Figure S7. Temperature variations of PSP NCs solution for six heating-cooling cycles, related to Figure 2.

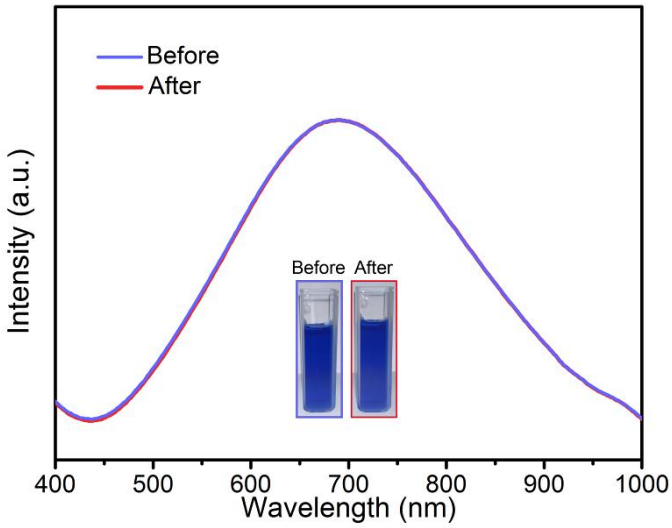

Figure S8. UV-vis-NIR spectroscopy of PSP NCs under the continuous irradiations of 671 nm laser. Inset: the representative photos of PSP NCs solution before and after irradiation for six heating-cooling cycles (the total irradiation time is 60 min), related to Figure 2.

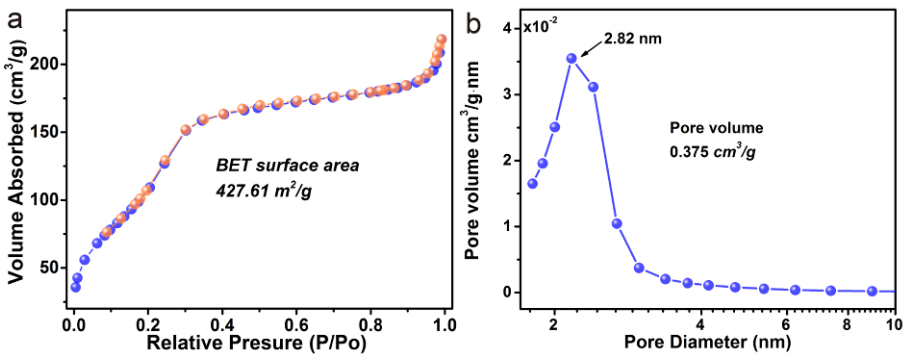

Figure S9. Nitrogen adsorption-desorption isotherms and pore size distributions of PSP NCs, related to Figure 2.

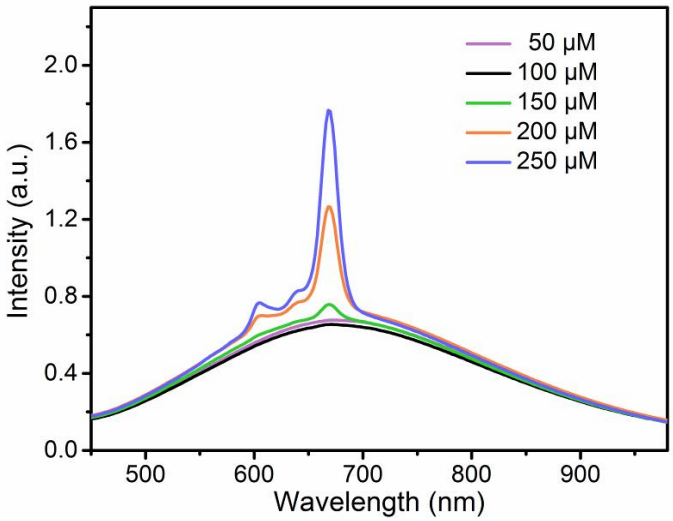

Figure S10. UV-vis spectra of PSPZP after loading ZnPc at different concentrations (5 mg of PSP NCs mixed with 1 mL of photosensitizer in DMSO solutions), related to Figure 2.

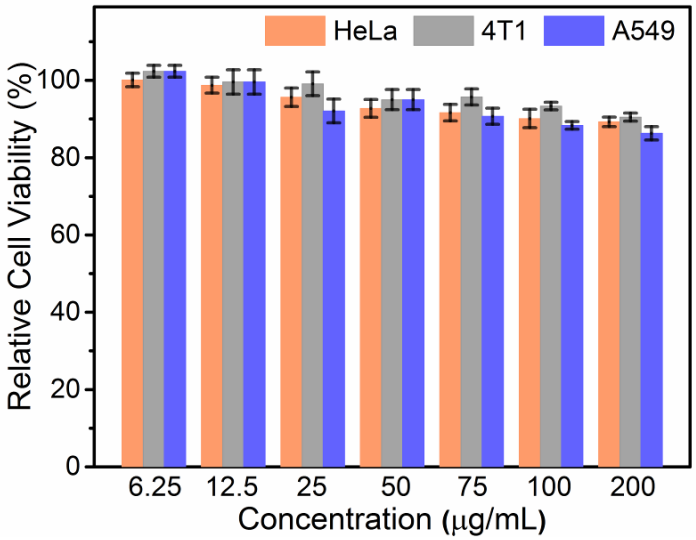

Figure S11. Viability of HeLa, 4T1 and A549 cells treated with PSP NCs at different concentrations, related to Figure 4.

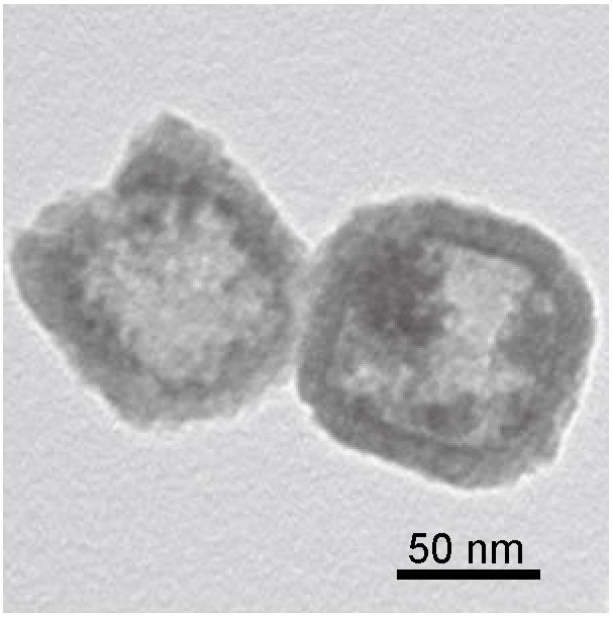

Figure S12. TEM images of mesoporous silica after the removal of inner Prussian blue, related to Figure 4.

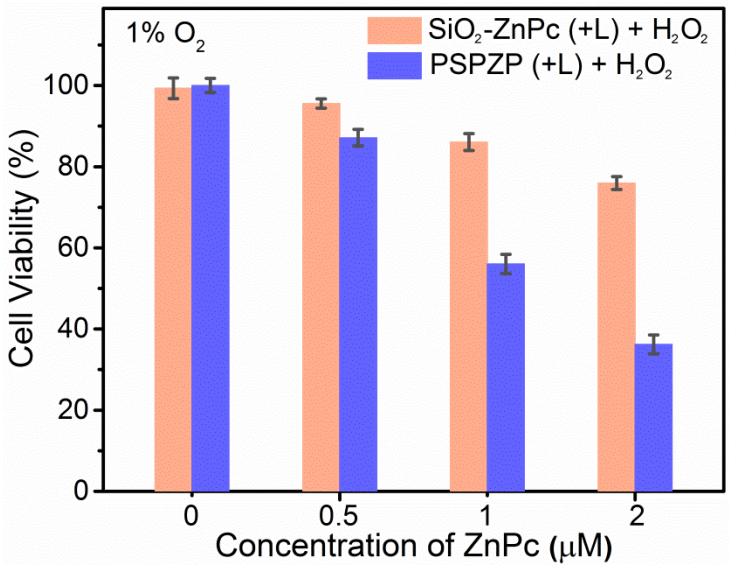

Figure S13. Viabilities of 4T1 cells treated with SiO_2-ZnPc or PSPZP NCs under NIR irradiation (671 nm, 0.4 W cm^{-2}, 5 min) in hypoxic condition, related to Figure 4.

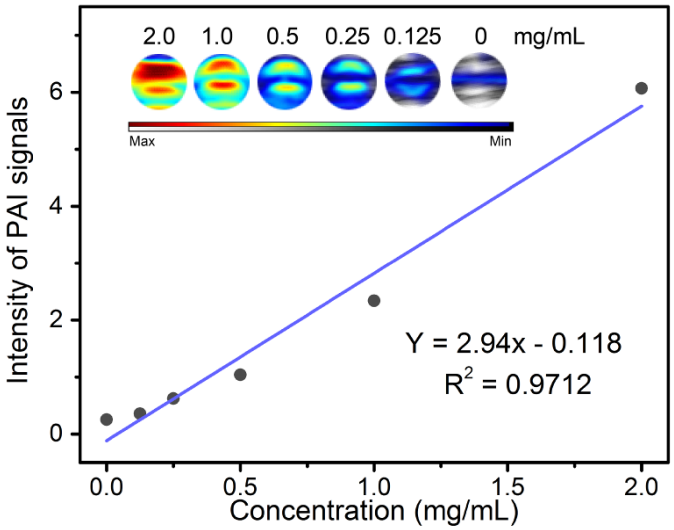

Figure S14. PA images of a series of PSP NCs solutions with different concentrations, related to Figure 5.

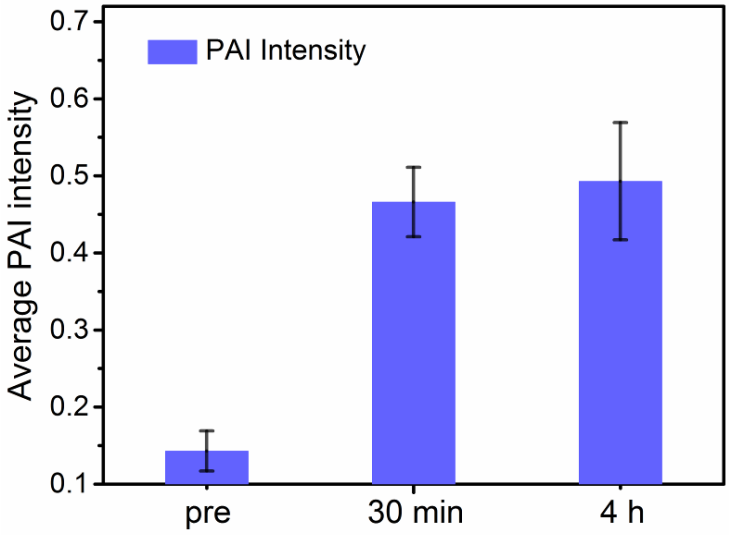

Figure S15. Temporal evolution of PA imaging signal of the tumor site, related to Figure 5.

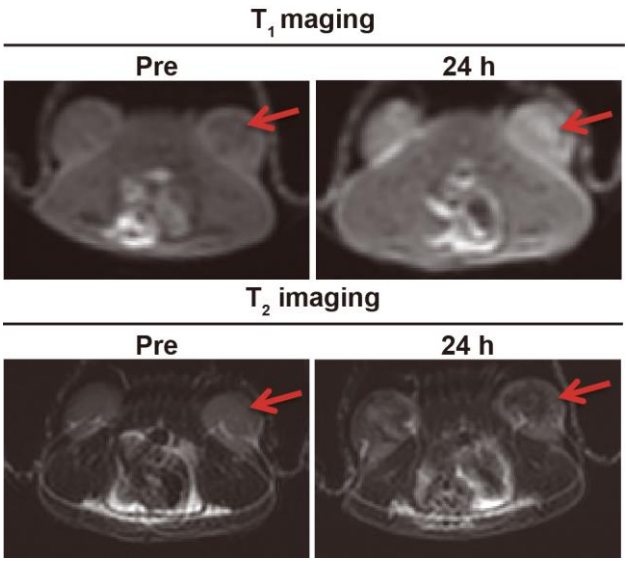

Figure S16. T_1- and T_2-weighted MR images of 4T1 tumor-bearing mice before and 24 hr after intravenous injection of PSP NCs, tumor marked by red arrows, related to Figure 7.

Transparent Methods

Materials Synthesis

All starting materials were obtained from commercial supplies and used as received. Potassium hexacyanoferrate ($K_3[Fe(CN)_6]$) and Zinc phthalocyanine (ZnPc) were purchased from Sigma-Aldrich (St. Louis, MO). 3-Aminopropyltriethoxysilane (APTES) was purchased from Alfa Aesar Reagent Company. Poly (vinylpyrrolidone (PVP, K-30), ammonia water ($NH_3 \cdot H_2O$), tetraethylorthosilicate (TEOS) and concentrated hydrochloric acid were purchased from Sinopharm Co. (Shanghai, China). Methoxy polyethylene glycol-maleimide (MAL-PEG-SCM, MW = 5000) was obtained from ToYongBio, Inc (China). 3-(4,5-dimethylthiazol-2-yl)-2,5-diphenyltetrazolium bromide (MTT) were purchased from Keygen Biotech. Co. (China).

Preparation of PSP NCs

First, PB nanoparticles were obtained according to our previous reports (Wang et al., 2016). ***Attention!!!:*** $C{\equiv}N^-$ containing chemicals may be produced and released during the acidic hydrothermal process. Typically, 50 mg Prussian blue nanoparticles (PB NPs) and 2 mL water were added in 20 mL of ethanol. Subsequently, 1 mL of ammonia (25%) were added. Then, 25 μL of TEOS were added quickly for preparing PB@sSiO_2. Thereafter, mesoporous silica was coated on the PB@sSiO_2 with the assistance of CTAB as the template. Typically, CTAB (0.12 g) and water (15 mL) were added in the above PB@sSiO_2 solution and stirred for 12 hr. Subsequently, 200 μL of TEOS and 280 μL of ammonia (25%) were added. After stirring at room temperature for 2 hr, the products were centrifuged and washed with ethanol three times. Finally, the PB@SiO_2 was refluxed and extracted in NH_4NO_3 ethanol solution (6 g/L) for 2 hr to remove the CTAB for three times. To further functionalize the mesoporous SiO_2 surface with -NH_2 groups, 10 mg of PB@SiO_2 NPs were first dispersed in 20 mL of absolute ethanol, followed by adding 1 mL of APTES. The system was sealed and kept at 80~90℃ in an oil bath for 48 hr. Afterward, the mixture was centrifuged and washed with ethanol several times to remove the residual APTES. Afterward, the 20 mg of PB@SiO_2-NH_2 was dispersed in a mixture containing MAL-PEG-SCM (50 mg) and ethanol (10 mL) and shook for 12 hr at room temperature. Finally, PB@SiO_2-PEG nanocatalyst (named as PSP NC) were obtained after washing with ethanol twice and dispersed in phosphate buffer solution (PBS) before subsequent studies. Also, the as-prepared PB@SiO_2 NPs were used to construct mesoporous silica through an etching process under alkaline solution. Then, the PEGylation modification process was the same as the PSP NCs.

Decomposition of H_2O_2 catalyzed by PSP NCs

The catalytic effect of PSP NCs was performed by mixing 1 mM of H_2O_2 and 2 mM of PSP NCs in PBS at 25, 37, 40 and 43℃. Then, 50 μL of the solution was added to 100 μL of $Ti(SO_4)_2$ solution (1.33 mL of 24% $Ti(SO_4)_2$+ 8.33 mL of H_2SO_4 in 50 mL of distilled water) every 30 min. The concentration of H_2O_2 was acquired by measuring the absorbance at 405 nm. The continuous catalytic effect was verified by repetitive addition of 1 mM of H_2O_2 to the solution, followed by measuring the concentration of H_2O_2 after incubation with PSP NCs under different temperature. To investigate the capability of evolving oxygen with the intracellular concentration of H_2O_2, 150 μM of H_2O_2 was incubated with 250 μM of PSP NCs in PBS, followed by measuring the O_2 concentration with an oxygen probe (JPBJ-608 portable Dissolved Oxygen Meters, Shanghai REX Instrument Factory).

Photosensitizer ZnPc loading

Zinc phthalocyanine (ZnPc) was chosen and dissolved in DMSO for further loading treatment. Loading

of ZnPc into PSP NCs was carried out by dispersing 5 mg of PSP in 1 mL of photosensitizer solutions (50~250 μM) and stirred for 12 hr without light interference at room temperature. The formed complexes PSP@ZnPc (named as PSPZP) were collected by centrifugation, washed with PBS 3 times. The contents of ZnPc were determined by the characteristic absorption at 671 nm. The weight amount of ZnPc loaded into PSP NCs was calculated by subtracting the ZnPc content in the supernatant from the total.

Singlet oxygen ($^1O_2$) detection

A chemical probe DPBF was used to confirm singlet oxygen by detecting its absorption intensity at 421 nm via UV-Vis spectroscopy (Lu et al., 2015). In a typical DPBF experiment, 30 μL DPBF in DMSO (10 mmol/L) was added to PSPZP solution (3 mL, 0.5 mmol/L). The solution was saturated with Ar atmosphere and kept in the dark and irradiated with a 671 nm laser (0.4 W cm^{-2}) for 30 min, and the absorption intensity of DPBF at 421 nm was recorded every 2 min. In the control experiments, DPBF absorption was recorded in water, and PSPZP plus H_2O_2 counterparts with or without 671 nm irradiation under different temperatures. Herein, hypoxic condition was achieved by Ar blowing into the solution for 30 min before test.

In vitro cellular experiments

HeLa human cervical cancer cells (HeLa), Human lung cancer cells (A549) and 4T1 murine breast cancer cells were originally obtained from American Type Culture Collection (ATCC) and cultured in standard cell media into 96-well plates and incubated in 5% CO_2 at 37℃ for 24 hr. Then different concentrations of PSP NCs were added into the 96-well plates and continued to be cultured for 24 hr. Cell viability was determined by the standard MTT assay. To study the cell killing efficacy of PTT, 4T1 cells seeded in 96-well plates were incubated with various concentrations of free PSP NCs for 4 hr with 671 nm laser at a power density of 0.4 W cm^{-2} for 5 min. For PDT, 4T1 cells seeded in 96-well plates were mixed with various concentrations of PSPZP and SiO_2-ZnPc with or without 100 μM H_2O_2 under normal (21% O_2, 5% CO_2 and 74% N_2) or hypoxic (1% O_2, 5% CO_2 and 94% N_2) environments. After 4 h, the 96-well plates were exposed to the 671 nm laser for 5 min. Then cells were transferred into fresh medium and further incubated for 24 hr. The standard MTT tests were then conducted to measure the relative cell viabilities. To further confirm the heat-assisted PDT efficacy, 4T1 cells were incubated with various concentrations of PSPZP with 100 μM H_2O_2 under different incubation temperatures. After 4 hr of incubation, the 96-well plates were exposed to the 671 nm light at a power density of 0.4 W cm^{-2} for 5 min. Then, cells were transferred into fresh medium and further incubated for 24 hr before the MTT assay.

Intracellular catalysis ability towards H_2O_2

Intracellular H_2O_2 assay (MAK164, Sigma Aldrich) was used to evaluate the intracellular H_2O_2 concentration after PSP NCs treatment. 100 μM of H_2O_2 was treated to 4T1 pre-incubated with PSP NCs for 24 hr, followed by incubation for 1 hr. Then, cell media was replaced by assay buffer and incubated for another 1 hr. After washing with PBS, intracellular H_2O_2 concentration was measured by fluorescent images (ex/em = 490/520).

Detection of intracellular O_2 generation

4T1 cells were seeded on Chambered cover glass (Lab-Tek Chambered 1.0 Borosilicate Cover Glass system, Nunc) (Xia et al., 2014). After 24 hr, the cells were cultured to 50-60% confluency, and incubated with PBS or PSP NCs at 37℃ under normal or hypoxic condition for 24 hr. Afterward, the cells in each group experienced their corresponding treatments. After 12 hr, these cells were then incubated with $[Ru(dpp)_3]Cl_2$ (Sigma-Aldrich, Co. Ltd.) at a concentration of 10 μg/mL for another 12

hr in a hypoxic incubator so as to evaluate the outcomes of continuous hypoxia modulation within 24 hr, followed by rinsing with PBS three times to remove the free $[Ru(dpp)_3]Cl_2$ and residual particles. The level of intracellular O_2 was evaluated by detecting the fluorescence of $[Ru(dpp)_3]^{2+}$ (λex = 450 nm, λem = 610 nm) by confocal laser scanning microscope (CLSM).

In vivo PA imaging, PET imaging and magnetic resonance imaging

For PA imaging, the 4T1 tumor-bearing mice were anesthetized and then injected with PSP NCs at a dose of 20 mg kg^{-1}. Then, at different time intervals post-injection (p.i.), the tumor region was imaged using the Endra Nexus 128 LAZER system with an excitation wavelength at 730 nm. For PET Imaging, ^{89}Zr-oxalate was produced according to previously reported procedures by the University of Wisconsin–Madison cyclotron group (Zhang et al., 2012). For chelator-free ^{89}Zr labeling, 1 mL of as-prepared PSP NCs in HEPES buffer (pH 7.0; 0.1 M) were mixed with 111 MBq ^{89}Zr oxalate and the pH was adjusted to 8-9 using Na_2CO_3 solution (2 M). The mixture was incubated at 70°C for 4 hr. After labeling, the labeling yield was determined by TLC at different time points. Final labeled products were collected by centrifugation. For *in vivo* PET imaging, 4T1 murine breast cancer cells were used for 4T1 tumor implantation when they reached ~80% confluence. All animal studies for PET imaging were conducted under a protocol approved by the University of Wisconsin Institutional Animal Care and Use Committee. The 4T1 tumor-bearing mice were used for *in vivo* experiments when the tumor diameter reached 6–8 mm. PET scanning at various time points (0.5, 3, 6, and 24 hr) after intravenous injection of 2~5 MBq of ^{89}Zr-PSP NCs were performed using a microPET/microCT Inveon rodent model scanner (Siemens Medical Solutions USA, Inc.). After the last scan at 24 hr p.i., biodistribution studies were carried out to confirm that the %ID/g values based on PET imaging truly represented the radioactivity distribution in mice. For *in vivo* MRI, 4T1-bearing mice were injected with PSP NCs (20 mg kg^{-1}) through the tail vein. Then, T_1 and T_2* MR imaging were performed before and 24 h after the intravenous injection with clinical magnetic resonance scanner (GE Signa HDxt 3.0 Tesla MRI system) equipped with a special animal imaging coil.

In vivo PTT assisted PDT therapy

The 4T1 tumor-bearing mice were randomly allocated into six group (n = 6): 1 is saline, 2 is PSPZP, 3 is NIR (671 nm, 0.4 W cm^{-2}, 5 min), 4 is ZnPc + NIR, 5 is PSP + NIR, 6 is PSPZP + NIR. The mice in the treatment groups were injected with saline, free ZnPc, PSP NCs, PSPZP solutions (total dose = 100 μL, $C_{[PSPZP]}$ = 2 mg mL^{-1}, the concentration of ZnPc and PSP NCs were based on the loading capacity) via the tail vein respectively. After 24 hr, the tumors from group 2, 3, 4 and 5 were irradiated with 671 nm laser (0.4 W cm^{-2}) for 5 min. The tumor dimensions were measured with a caliper, and the tumor volume was calculated according to the equation: Volume of tumor was calculated as $V = a \times b^2/2$, where “a” and “b” were the longest and shortest diameters of the tumor, respectively. The body weight of mice was recorded at 2 day intervals. Relative tumor volume was normalized to its initial size before administration and laser irradiation. All mice were sacrificed after experiment and tumors of each group were collected.

Histology examination

After *in vivo* therapy experiments, the tumor tissues harvested from the administrated mice were fixed in 10% formalin, dehydrated with gradient ethanol, embedded in paraffin and sectioned. Then the tumor sections were stained with hematoxylin and eosin (H&E) for the detection of changes in the cellular integrity and tissue morphology and anti-Ki-67 rabbit polyclonal antibody (Abcam, ab15580, America) for the detection of proliferative cells. Finally, the images of the stained tumor slices were characterized using Olympus IX-70 microscope.

Immunofluorescence staining

To study the change of hypoxia within tumor microenvironment after intravenous injection with PSP NCs (10 mg kg^{-1}). 1.5 hr before tumors surgically excised from the mice (24 hr post injection of PSP solution), the mice were intraperitoneally injected with pimonidazole hydrochloride (Hypoxyprobe, USA) at a dose of 30 mg kg^{-1} according to the procedure provided by the manufacturer. The collected tumor slices were firstly stained with mouse anti-pimonidazole monoclonal antibody and rat anti-mouse CD31 antibody as primary antibodies to label tumor hypoxia regions and blood vessels, respectively. Then the slices were stained with Alex 488-conjugated goat anti-mouse secondary antibody and rhodamine-conjugated donkey anti-rat secondary antibody, respectively. Finally, the images of stained slices were characterized using CLSM (Zeiss LSM 710). The hypoxia region and the density of blood vessels of each slice were statistically analyzed using the Imaging-J software.

Hematological analysis and in vivo biocompatibility test

Healthy female Bale/c mice were divided into two groups and injected with saline and PSPZP (100 μL, 2 mg mL^{-1}), respectively. At 7 and 15 days after intravenous injection, blood samples were collected from the tail artery for blood chemistry tests (ALT, ALP, AST and BUN) and routine blood analysis (RBC, WBC, HGB, MCHC, PLT, MCH, MPV, MCV, HCT). For testing *in vivo* biocompatibility of PSPZP. 4T1 tumor bearing mice were treated with saline, PB, mesoporous SiO_2, PSP or PSPZP for 120 hr, respectively. Then the sections of main organs (heart, kidney, liver, lung, spleen) were stained with hematoxylin and eosin (H&E) for the detection of changes in the cellular integrity and tissue morphology.

Characterization

The interaction and microstructure of particles were analyzed by an FT-IR spectrometer (Nicolet 8700, Nicolet Co., USA) and X-ray diffraction (XRD) (TTR-III, Rigaku Co., Japan). The morphology was analyzed with an H-7650 TEM (Hitachi Co., Japan) and a JSM-6700 M SEM (JEOL Co., Japan). The elements distribution was characterized using a STEM with EDX spectroscopy (JEM-2100F, JEOL Co., Japan). ICP measurements were carried out on an ICP-AES (Optima 7300DV, PerkinElmer Co., USA). The BET specific surface areas and pore size distribution were measured using a porosimetry analyzer (ASAP 2020, Micromeritics, USA). The UV-Vis absorption spectra were measured on an ultraviolet-visible absorption spectrometer (SOLID 3700, Shimadzu, Japan). The temperature was measured using a digital non-contact Infrared Thermometer with a resolution of 0.1℃. Particle size distribution measurements were conducted on a DLS detector (Zetasizer uV, Malvern, UK).

Supplemental References:

Wang, D., Zhou, J., Chen, R., Shi, R., Zhao, G., Xia, G., Li, R., Liu, Z., Tian, J., Wang, H., Guo Z., Wang, H. and Chen, Q. (2016). Biomaterials *100*, 27-40.

Lu, S., Tu, D., Hu, P., Xu, J., Li, R., Wang, M., Chen, Z., Huang, M., and Chen, X. (2015). Angew. Chem., Int. Ed. *54*, 7915-7919.

Xia, P., Zhou, J., Song, X., Wu, B., Liu, X., Li, D., Zhang, S., Wang, Z., Yu, H., Ward, T., Zhang, J., Li, Y., Wang, X., Chen, Y., Guo, Z., Yao, X. (2014). Journal of molecular cell biology *6*, 240-254.

Zhang, Y., Hong, H., Severin, G.W., Engle, J.W., Yang, Y., Goel, S., Nathanson, A.J., Liu, G., Nickles, R.J., and Leigh, B.R. (2012). Am J Transl Res *4*, 333-346.